

[nature](#) > [nature cell biology](#) > [resources](#) > [article](#)

Resource | Published: 23 December 2019

# Mapping the proximity interaction network of the Rho-family GTPases reveals signalling pathways and regulatory mechanisms

[Halil Bagci](#), [Neera Sriskandarajah](#), [Amélie Robert](#), [Jonathan Boulais](#), [Islam E. Elkholi](#), [Viviane Tran](#), [Zhen-Yuan Lin](#), [Marie-Pier Thibault](#), [Nadia Dubé](#), [Denis Faubert](#), [David R. Hipfner](#), [Anne-Claude Gingras](#) & [Jean-François Côté](#) 

*Nature Cell Biology* **22**, 120–134 (2020)

**15k** Accesses | **90** Citations | **93** Altmetric | [Metrics](#)

 An [Author Correction](#) to this article was published on 10 February 2020

 This article has been [updated](#)

## Abstract

Guanine nucleotide exchange factors (RhoGEFs) and GTPase-activating proteins (RhoGAPs) coordinate the activation state of the Rho family of GTPases for binding to effectors. Here, we exploited proximity-dependent biotinylation to systematically define the Rho family proximity interaction network from 28 baits to produce 9,939 high-confidence proximity interactions in two cell lines. Exploiting the nucleotide states of Rho GTPases, we revealed the landscape of interactions with RhoGEFs and RhoGAPs. We systematically defined effectors of Rho proteins to reveal candidates for classical and atypical Rho proteins. We used optogenetics to demonstrate that KIAA0355 (termed GARRE here) is a RAC1 interactor. A functional screen of RHOG candidate effectors identified PLEKHG3 as a promoter of Rac-mediated membrane ruffling downstream of RHOG. We identified that active RHOA binds the kinase SLK in

*Drosophila* and mammalian cells to promote Ezrin–Radixin–Moesin phosphorylation. Our proximity interactions data pave the way for dissecting additional Rho signalling pathways, and the approaches described here are applicable to the Ras family.

## Main

---

The large Ras superfamily regulates biological processes including proliferation, cytoskeletal dynamics and vesicular trafficking<sup>1</sup>. The Rho family is composed of 20 proteins that regulate cytoskeletal dynamics<sup>2</sup>. Rho proteins are molecular switches cycling between inactive GDP-bound and active GTP-bound states<sup>3</sup>. The RhoGEFs promote the dissociation of GDP from Rho proteins to allow GTP loading<sup>4,5</sup>. RhoGAPs recognize GTP-loaded Rho proteins to promote their intrinsic GTPase activity<sup>6</sup>. Active Rho proteins adopt a conformation that enables coupling to effector proteins that propagate signal transduction events<sup>7</sup>. Dysregulation of their activity leads to a spectrum of diseases<sup>8,9,10</sup>.

The classical Rho GTPase subfamilies RhoA (comprising RHOA–RHOC), Rac (comprising RAC1–RAC3 and RHOG), Cdc42 (comprising CDC42, RHOJ and RHOQ) and RhoF (comprising RHOD and RHOF) are regulated by GDP/GTP exchange<sup>11</sup>. Four Rho subfamilies are considered atypical. RHOU and RHOV are fast-cycling GTPases that are found loaded with GTP in cellulo<sup>2</sup>. Rnd (comprising RND1–RND3) and RHOH proteins lack GTPase activity and are constitutively active<sup>11</sup>. RHOBTB1 and RHOBTB2 harbour divergent GTP-binding domains flanked by carboxy-terminal extensions. Despite the simplicity of the on/off switch model, the regulation of Rho proteins is complicated by the presence of 80 RhoGEFs<sup>4</sup>, 69 RhoGAPs<sup>6</sup> and multiple effector proteins that together vastly exceed the number of Rho proteins. Hence, most studies focus on single RhoGEF, RhoGAP, Rho and/or effector pathways, with the functions of RHOA, RAC1 and CDC42 understood in greater detail. The exact specificity of GEFs and GAPs, and whether they are selective or promiscuous towards Rho proteins, remains a key question<sup>12</sup>. The repertoire of Rho effectors is large and incomplete, raising the question of which signals guide Rho proteins to activate specific effector pathways. These gaps in knowledge apply to all Ras proteins, which limits our understanding of their signalling activities.

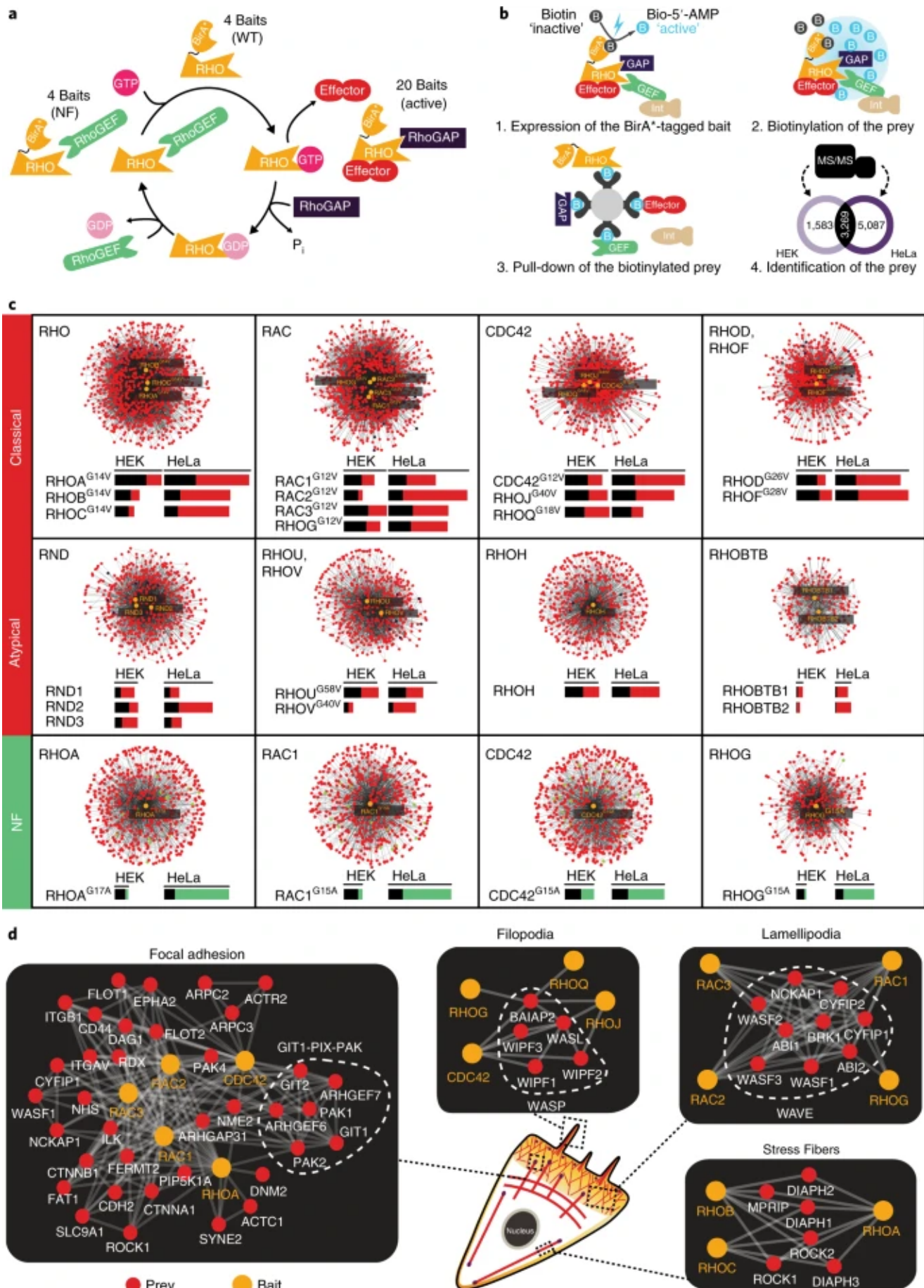
Here, we systematically define the Rho-family interactome using proximity-dependent biotinylation (BioID). The screens use the following Rho proteins: nucleotide-free Rho proteins, which have increased affinity towards GEFs; constitutively active Rho proteins, which are prone to interact with effector proteins and GAPs; and wild-type (WT) proteins as activity controls. We reveal the specificity of GEFs and GAPs and present the landscape of effector complexes for Rho proteins. Our Rho BioID platform provides a resource of high-confidence proximal protein interactions that are exploitable to uncover components involved in cytoskeletal dynamics or unexpected functions of Rho proteins.

## Results

A BioID pipeline to systematically define proximity interaction networks of the Rho family

Rho proteins engage in protein–protein interactions with their regulators and effectors to carry out their functions (Fig. 1a). Because these interactions are dynamically regulated and implicate components of the cytoskeleton and membrane systems, they have been challenging to assess using standard biochemical methods. We focus on the BioID approach that has demonstrated usefulness in such contexts<sup>13</sup>. BioID exploits an abortive *Escherichia coli* biotin ligase (BirA\*) fused to a bait that biotinylates proteins in close proximity<sup>14</sup> (Fig. 1b).

**Fig. 1: The large-scale Rho GTPases proximity interaction network.**



**a**, The Rho cycle and the strategy used to define the interactome of Rho family members by BiOID coupled to MS. A total of 20 active, 4 nucleotide-free (NF; RHOA, RAC1, RHOG, CDC42) and 4 WT (RHOA, RAC1, RHOG, CDC42) Rho GTPases were fused with the abortive biotin ligase BirA\*. Constitutively active Rho baits are predicted to specifically label effectors and

RhoGAPs, whereas NF baits are expected to label RhoGEFs. WT baits are used as activity controls. **b**, Workflow of the BiOID approach performed in Flp-In T-REx HEK293 and HeLa cell lines. The expression of each bait was induced by tetracycline for 24 h in the presence of biotin (1), which led to the BirA\*-mediated biotinylation of proteins in proximity to the bait (2). An example of a proximal interactor that is not biotinylated is shown (Int). The biotinylated proteins were isolated from solubilized cell extracts (3) and identified by MS (4). SAINT express analyses were performed on the following sample sizes (number of interactions):  $n = 5,381$  for NF in HEK,  $n = 7,462$  for NF in HeLa,  $n = 17,548$  for active in HEK and  $n = 22,042$  for active in HeLa. Only proximity interactions displaying an AvgP  $\geq 0.95$  assessed by SAINT express (below the Bayesian 1% false-discovery rate (FDR) estimate) were kept and deemed of high confidence. A total of 9,939 high-confidence interactions are enumerated in a Venn diagram, which displays the amount of unique proximity interactions identified in HEK293 (light purple circle) and HeLa (dark purple circle), or proximity interactions identified in both cell lines (dark grey). **c**, Graphical representation of the interaction networks of active (red) and NF (green) baits are organized according to the classification of Rho subfamilies. Red and green bars represent the relative levels of unique interactions (AvgP  $\geq 0.95$  assessed by SAINT express) for each bait in each cell line, while black bars represent the levels of interactors identified in both cell lines. The data are available as Cytoscape files (Supplementary Data 1). **d**, Multiple established Rho effector complexes involved in lamellipodia formation, generation of filopodia, establishment of stress fibres and focal adhesion modulation were identified by BiOID, thereby validating the approach.

We took advantage of BiOID to define the interaction of Rho proteins with their GEFs and GAPs and to better define their effector landscapes (Fig. 1a). To identify interactions with GEFs, we reasoned that nucleotide-free forms of Rho proteins would be ideal to map these events<sup>15</sup>. We focused on the classical Rho proteins RAC1, RHOG, CDC42 and RHOA as surrogates for these subfamilies; atypical Rho proteins were excluded, as they do not require GEFs. To identify associations with GAPs and effectors, we reasoned that constitutively active forms of Rho proteins would enrich for such proteins<sup>6,7</sup>. Constitutively active mutants have a mutation in a critical amino acid required for GTP hydrolysis (G12V in RAC1) and are locked in a GTP-loaded form<sup>16</sup>. Classical Rho proteins and fast-cycling RHOU and RHOV were profiled in their constitutively active forms, while atypical RND1–RND3, RHOH, RHOBTB1 and RHOBTB2 were profiled WT as they are GTPase-dead. To evaluate the impact of such

mutations, we also profiled the classical Rho proteins RAC1, RHOG, CDC42 and RHOA in WT forms. Since WT GTPases cycle between active and inactive states, they transiently bind to GEFs, GAPs and effectors. We expected WT baits to have prey in common with their nucleotide-free or constitutively active homologues, although with lower spectral counts, thereby making them activity controls. BirA\*-Flag, BirA\*-Flag-enhanced green fluorescent protein (eGFP) and a membrane-targeted BirA\*-Flag-eGFP, via fusion of a CAAX motif, were used as controls to filter out contaminants (see [Methods](#)). These baits and associated mutations are described in Supplementary Table 1. Expression of the baits in Flp-In T-REx HEK293 and HeLa cells was confirmed by western blotting (Extended Data Fig 1). The expression levels of BirA\*-Flag-RAC1 and BirA\*-Flag-CDC42, as surrogates for all baits, were estimated to be twofold to threefold higher than endogenous proteins (Extended Data Fig 1c). These baits induced cytoskeletal changes and biotinylation of proteins when expressed (Extended Data Fig. 2), thereby confirming that they are appropriate for BioID screens.

The proximity interactome of the Rho family of GTPases BioID coupled to mass spectrometry (MS) screens with 28 Rho baits (Supplementary Table 1) were conducted in HEK293 and HeLa Flp-In T-REx cells to maximize the coverage of proximal interactions for each bait (Fig. 1a,b). We selected HEK293 cells as they are widely used for standard proteomics, including the first release of BioPlex (<https://bioplex.hms.harvard.edu>), which makes benchmarking easier. HeLa cells were selected as a classical model for Rho signalling and for microscopy analyses. These screens detected 9,939 proximity interactions, with 3,269 proximity interactions detected in both cell lines (Fig. 1c; the interactomes depicted are available as Cytoscape files (Supplementary Data 1); Supplementary Tables 7–10; [Methods](#)). The overlap of our proximity interactions with the literature was low, with 1.8% of our proximity interactions previously reported in BioGRID (<https://thebiogrid.org>), which is consistent with other BioID studies [17,18,19,20](#). These 180 previously reported interactions enabled us to attest that our approach recapitulated known specificity across the Rho family. As examples, active RAC1–RAC3 baits identified all components of WAVE complexes (WASF1–WASF3, ABI1, ABI2,

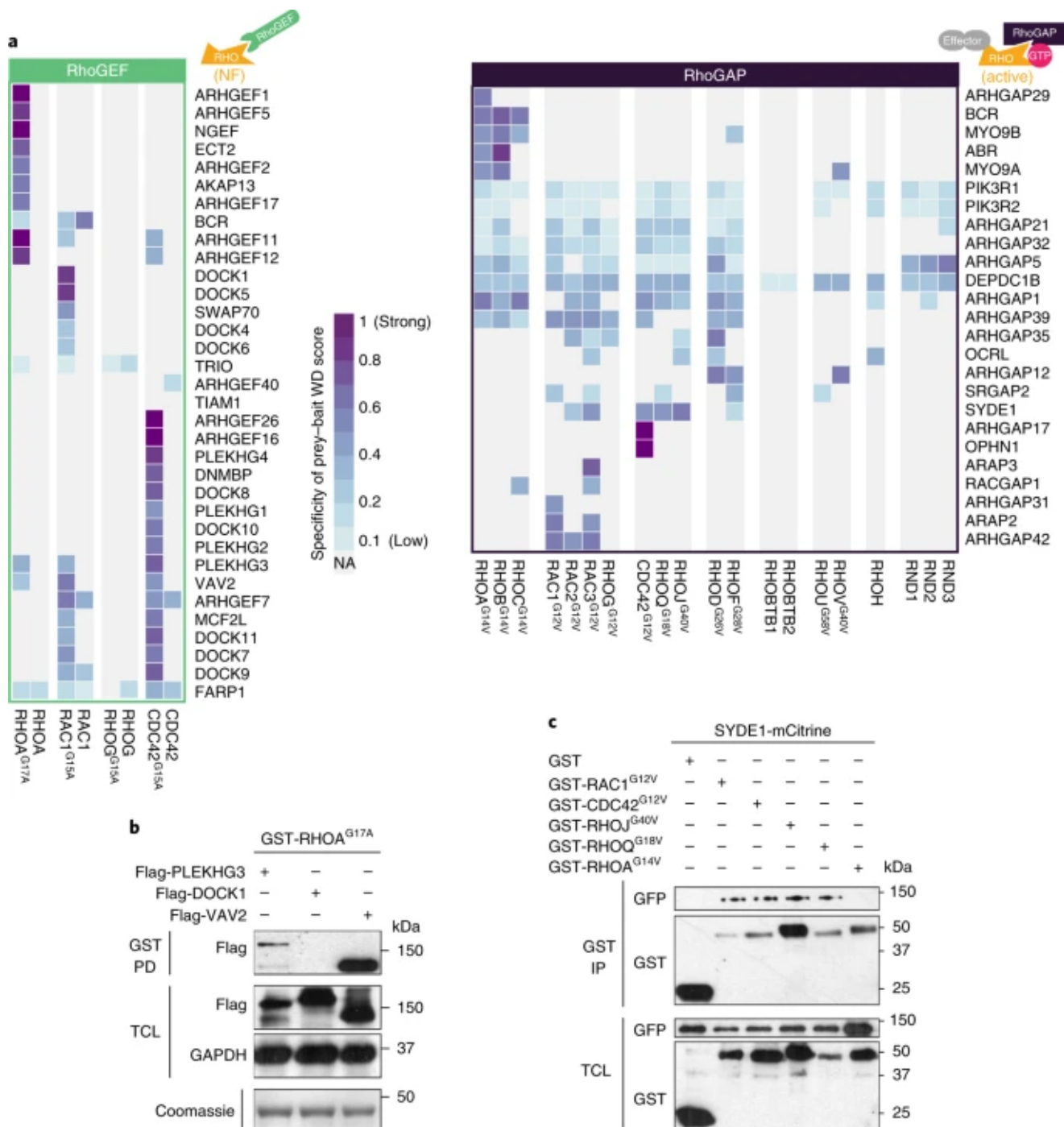
NCKAP1, CYFIP1, CYFIP2 and BRK)<sup>21</sup> (Fig. 1d), which are key for lamellipodia formation (Extended Data Fig. 2). Active CDC42 bait identified WIPF1–WASF3 in complexes with WAFL<sup>22</sup> (Fig. 1d), which contribute to the generation of filopodia (Extended Data Fig. 2). Active RHOA–RHOC baits identified ROCK1–ROCK2–MPRIP<sup>23</sup> and DIAPH1–DIAPH3 (ref. 24) complexes (Fig. 1d), which are important in forming stress fibres (Extended Data Fig. 2). Proximal interactions of CDC42 and Rac with proteins involved in focal adhesion turnover were identified (Fig. 1d). A dotplot analysis from the four classical Rho proteins confirmed marked differences between WT and constitutively active baits to retrieve known effectors (Extended Data Fig. 3a), thus justifying the use of active forms of Rho proteins to identify effectors. These data are available for mining by the research community via ProHits at [http://prohits-web.lunenfeld.ca/GIPR/Datasets.php?projectId=25&m\\_num=m3/](http://prohits-web.lunenfeld.ca/GIPR/Datasets.php?projectId=25&m_num=m3/).

Defining the landscape of interactions of Rho proteins with GEFs

We compared interactions of nucleotide-free classical Rho proteins (RAC1<sup>G15A</sup>, RHOG<sup>G15A</sup>, CDC42<sup>G15A</sup> and RHOA<sup>G17A</sup>) and their WT forms (Fig. 2a). In all but one case, the nucleotide-free form interacted with more GEFs than the WT protein. Some GEFs displayed specificity for one of the baits, which recapitulates previous reports as follows. RHOA<sup>G17A</sup> interacted with the RHOA-specific GEFs ARHGEF1 (ref. 25), ARHGEF2 (ref. 26), ARHGEF5 (ref. 27), ARHGEF17 (ref. 28), NGEF<sup>29</sup>, ECT2 (ref. 30) and AKAP13 (ref. 31) (Fig. 2a). RAC1<sup>G15A</sup> bound the RAC1-specific GEFs SWAP70 (ref. 32), DOCK1 (refs. 33,34), DOCK4 (ref. 35), DOCK5 (ref. 36) and DOCK6 (ref. 37). Finally, CDC42<sup>G15A</sup> interacted with the CDC42-specific GEFs DNMBP<sup>38</sup>, PLEKHG1 (ref. 39), DOCK8 (ref. 40) and DOCK10 (ref. 41) (Fig. 2a). BiOID confirmed the reported broad selectivity of some GEFs as follows: VAV2 (ref. 42) for RHOA, RAC1 and CDC42; TRIO<sup>43</sup> for RHOA, RAC1 and RHOG; ARHGEF11 (ref. 44) for RHOA, RAC1 and CDC42; DOCK7 (ref. 45) for RAC1 and CDC42; ARHGEF7 (ref. 46) for RAC1 and CDC42; FARP1 (ref. 47) for RHOA, RAC1 and CDC42; and BCR<sup>48</sup> for RHOA and RAC1 (Fig. 2a). We detected an interaction between CDC42<sup>G15A</sup> and ARHGEF26, which is believed to be a RHOG-specific GEF. Notably, the initial studies of ARHGEF26 reported activity towards CDC42 (ref. 49). While we found that RHOA<sup>G17A</sup> interacted with its established GEF ARHGEF12 (ref. 50), an interaction with CDC42<sup>G15A</sup> was also detected (Fig. 2a), which

suggests that it may have broader activity than reported. PLEKHG3 is validated as a RAC1 and CDC42 GEF<sup>51</sup>, and our BiOID data confirmed this specificity, but also revealed binding to RHOA. We experimentally confirmed that PLEKHG3 interacts with nucleotide-free RHOA, which suggests that it is also a RHOA GEF (Fig. 2b). Hence, nucleotide-free Rho baits are effective for uncovering the GEFs that regulate them.

**Fig. 2: Mappings of RhoGEF and RhoGAP specificities.**



**a**, Rho baits in NF and active forms detect RhoGEFs (left) and RhoGAPs (right), respectively. Heatmaps represent the relative specificities (cells-combined WD score) of identified RhoGEFs and RhoGAPs towards each respective NF and active baits. Baits are organized

according to the classification of Rho subfamilies. SAINT express analyses were performed on the following sample sizes (number of interactions):  $n = 5,381$  for NF in HEK,  $n = 7,462$  for NF in HeLa,  $n = 17,548$  for active in HEK and  $n = 22,042$  for active in HeLa. Only proximity interactions displaying an AvgP  $\geq 0.95$  (below the Bayesian 1% FDR estimate) were kept and deemed of high confidence. WD scorings were next performed on these high-confidence interactions. NA, no spectral counts available. **b**, GST pulldown (PD) assays were performed in lysates from Flp-In T-REx HEK293 cells expressing Flag-PLEKHG3, Flag-DOCK1 (negative control) or Flag-VAV2 (positive control) incubated with purified GST-RHOA<sup>G17A</sup>. GAPDH was used as the loading control. TCL, total cell lysates. The Coomassie staining shows purified GST-RHOA<sup>G17A</sup>. Data are representative of three independent experiments. **c**, SYDE1 binds to multiple active Rho GTPases, including the atypical RHOJ and RHOQ. HeLa cells were transfected with SYDE1-mCitrine together with the indicated GST fusions, and GST pull-down and immunoprecipitation (IP) assays were performed. Data are representative of three independent experiments. Unmodified scans related to **b** and **c** are available as source data.

#### Source data

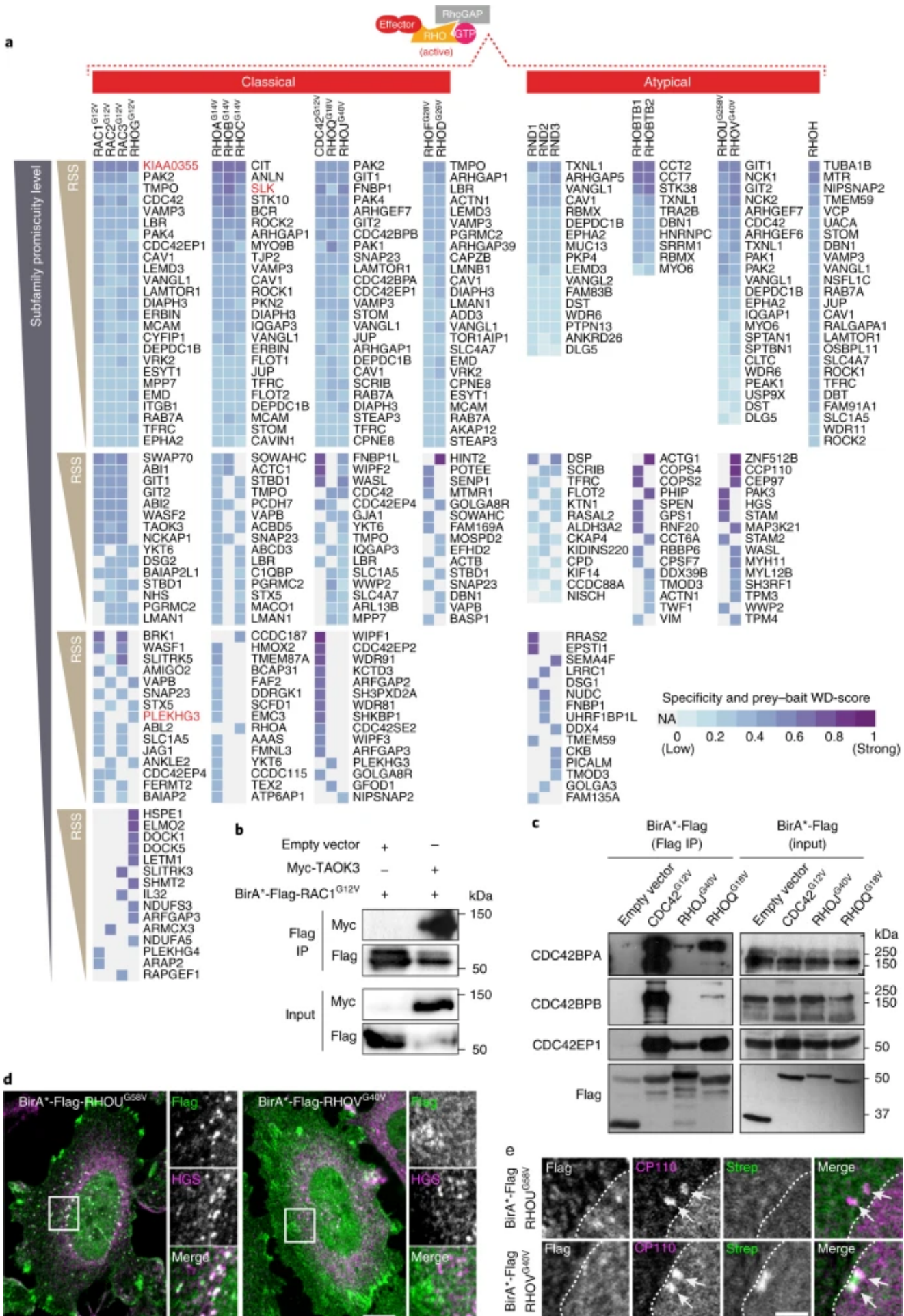
### Defining the landscape of interactions of Rho proteins with GAPs

As a proof of principle for using active Rho mutants to identify specific GAPs, we compared interactions of active forms of classical Rho proteins (RAC1<sup>G12V</sup>, RHOG<sup>G12V</sup>, CDC42<sup>G12V</sup> and RHOA<sup>G14V</sup>) versus WT counterparts. As the interactions between WT forms and GAPs are transient, the average spectral count (AvgSpec) and relative abundance of GAPs retrieved with WT baits were lower than corresponding active baits, which shows that GAPs were enriched in active Rho baits (Extended Data Fig. 3b). On the basis of this result, we broadly profiled all active Rho proteins to assess the specificity of GAPs for individual family members. RhoGAP domains are described to be promiscuous<sup>52</sup>, and ~40% of GAPs detected indeed displayed broad interaction patterns with Rho GTPases (for example, ARHGAP1, ARHGAP5, ARHGAP21, ARHGAP32 and ARHGAP39) (Fig. 2a). We found that multiple GAPs displayed restricted patterns of interaction with Rho proteins, several of which are consistent with literature reports. This includes ARAP2, RACGAP1 and ARHGAP31 with RAC1–RAC3 proteins<sup>53,54,55</sup>, ARHGAP17 with CDC42 (ref. 56), MYO9A, MYO9B and ARHGAP29 with the RHOA subfamily<sup>57,58</sup>, and RND1–RND3 GTPases with ARHGAP5

(ref. [59](#)) (Fig. [2a](#)). Among the uncharacterized proximity interactions, we found that the CDC42 RhoGAP SYDE1 was not only recovered with CDC42 (ref. [60](#)), but also with RHOQ and RHOJ (Fig. [2a](#)). While not all BioID proximity interactions indicate direct protein interactions, or common membership to a protein complex, we opted to experimentally assess whether this was the case for this RhoGAP using a pull-down assay. Glutathione S-transferase (GST)-tagged constitutively active CDC42, RHOQ and RHOJ, but not RHOA, precipitated mCitrine-SYDE1 (Fig. [2c](#)). These screens therefore provide a previously unreached view of the interplay of GAPs with the Rho family of proteins.

Active Rho-subfamily proximity interactions reveal the effectors landscape To identify the prey that were most enriched for each active Rho subfamily, we assigned each prey a Rho-subfamily score (RSS; [Methods](#)). We provide the top interactors, that is, those with the highest RSS through different levels of subfamily promiscuity, for each Rho subfamily (Fig. [3a](#)). As examples, we note that the top interactors for RHOA–RHOC include known effectors, including CIT, ROCK1 and ROCK2 (Fig. [3a](#)). CDC42 subfamily proteins were found to interact with established effectors, including PAK2 complexes (PAK1–PAK2 and GIT1–GIT2) and PAK4 (Fig. [3a](#)). Within the Rac subfamily, RAC1–RAC3, but not RHOG, bound to the WASF2 complex<sup>[21](#)</sup>, while RHOG, but not RAC1–RAC3, bound to ELMO2 (ref. [61](#)) (Fig. [3a](#)).

### Fig. 3: Mappings and identifications of Rho-family-specific candidate effectors.



**a**, Active forms of Rho GTPases binds effectors. Heatmaps display the top Rho GTPases–prey interactions specificities (cells-combined WD score) and are regrouped by Rho GTPase

phylogenetic subfamilies. Dark purple squares indicate the strongest bait–prey specificities, whereas grey squares are unidentified preys. Candidate effectors are segregated into groups of subfamily promiscuity level (up to four levels depending on the subfamily size) and ordered decreasingly according to their RSS ([Methods](#)). From this subfamily classification and ordering approach, KIAA0355, SLK and PLEKHG3 (in red) were identified as candidate effectors. NA, no spectral counts available. SAINT express analyses were performed on the following sample sizes (number of interactions):  $n = 5,381$  for NF in HEK,  $n = 7,462$  for NF in HeLa,  $n = 17,548$  for active in HEK and  $n = 22,042$  for active in HeLa. Only proximity interactions displaying an AvgP  $\geq 0.95$  (below the Bayesian 1% FDR estimate) were kept and deemed of high confidence. WD scorings were next performed on these high-confidence interactions. See Supplementary Table [11](#) for the entire dataset. **b**, TAO3 binds the active form of RAC1. Western blots show the co-immunoprecipitation of Myc-TAO3 with BirA\*-Flag-Rac1<sup>G12V</sup> from HeLa cell lysates. Data are representative of three independent experiments. **c**, Western blots show the co-immunoprecipitation of endogenous CDC42BPA, CDC42BPB and CDC42EP1 with the indicated BirA\*-Flag-tagged CDC42 family members from HeLa cell lysates. Data are representative of four independent experiments. Unmodified scans related to **b** and **c** are available as source data. **d**, Confocal images of anti-Flag and anti-HGS immunostaining show that the active form of RHOU (left; the three smaller images to the right are magnified images of the area outlined by the white square), but not of RHOV (right; the three smaller images to the right are magnified images of the area outlined by the white square), localizes to HGS-positive endosomes. Data are representative of two independent experiments. Scale bar, 10  $\mu\text{m}$  (applies to all images). **e**, Active RHOV, but not RHOU, interacts with the centrosomal protein CP110 but do not accumulate at the centrosome. Confocal images of anti-Flag and anti-CP110 immunostaining together with streptavidin (Strep) staining are shown. Data are representative of two independent experiments. The arrows point to the centrioles and the broken line delineates the nucleus. Scale bar, 2  $\mu\text{m}$  (applies to all images).

#### [Source data](#)

Among the uncharacterized interactions specific for subfamilies of classical Rho proteins, TAO3 was identified as a proximity interactor of RAC1–RAC3 (Fig. [3a](#)). The interaction of RAC1<sup>G12V</sup> with TAO3 was biochemically confirmed (Fig. [3b](#)). Within the CDC42 subfamily, we revealed a series of CDC42-binding proteins as candidate effectors of RHOQ and RHOJ, including FNBP1, CDC42BPA, CDC42BPB and CDC42EP1 (Fig. [3a](#)). While CDC42 bound to CDC42BPA, CDC42BPB and CDC42EP1 as expected,

we biochemically confirmed the interaction of CDC42BPA, CDC42BPB and CDC42EP with RHOQ (Fig. 3c).

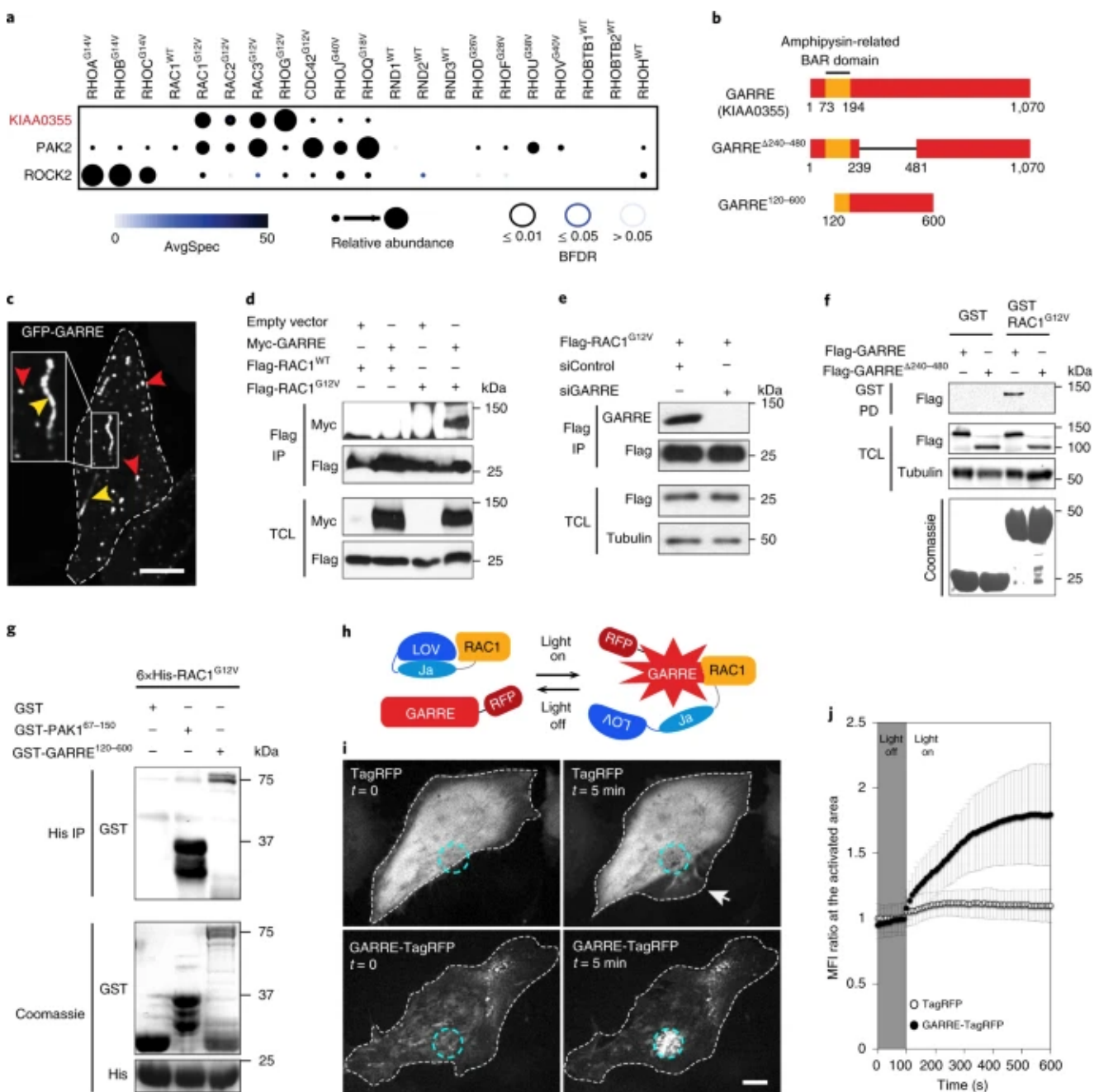
Atypical RHOU and RHOV uniquely harbour amino-terminal regions containing proline-rich motifs that bind to the SH3-domain-containing NCK1 and NCK2 proteins, which were prominent in our screen data (Fig. 3a). RHOU and RHOV were found to interact with classical PAK complexes (PAK1 and PAK2 and GIT1 and GIT2) while PAK3 bound RHOU (Fig. 3a). Among the uncharacterized candidates, RHOU was proximal to HGS, STAM1 and STAM2, which are components of the ESCORT complex, thus suggesting that RHOU may regulate aspects of endosomal trafficking (Fig. 3a). While, no biochemical interaction was detectable, colocalization of RHOU, but not RHOV, with HGS on endomembranes was observed (Fig. 3d). RHOV, which is reported to localize at the plasma membrane and on endomembranes<sup>62</sup>, recovered CEP97–CP110 that regulates ciliogenesis<sup>63</sup> (Fig. 3a). While we could not detect a biochemical interaction, we noted a colocalization of RHOV-induced biotinylation with CP110 at the centrosome (Fig. 3e), which suggests that there was a transient localization of RHOV in CP110-containing complexes. These results demonstrate that our datasets can identify candidates for both direct and labile interactions of the Rho family of proteins using traditional methods.

GARRE is an interactor of active Rac subfamily of GTPases

We identified KIAA0355 with the highest RSS in the Rac family (Figs. 3a and 4a). KIAA0355 showed increased interactions with constitutively active Rac proteins in comparison to WT baits (Fig. 4a). We have previously reported that KIAA0355 establishes proximal interactions to proteins localized in RNA processing bodies<sup>17</sup>. We rename this protein as granule-associated Rac and RHOG effector (GARRE). Phylogenetic analyses revealed that GARRE appeared late in evolution, as it is restricted to vertebrates (Extended Data Fig. 4a). The human protein is composed of 1,070 amino acids and contains a predicted BAR domain (Fig. 4b; Extended Data Fig. 4b). A DUF4745 domain overlaps with this BAR domain (Extended Data Fig. 4c). We found that GFP-GARRE accumulated in granule-like puncta (Fig. 4c, red arrows) that sometimes aligned along structures reminiscent of tubular membranes (Fig. 4c,

yellow arrows). We confirmed that Myc-GARRE co-immunoprecipitates specifically with Flag-RAC1<sup>G12V</sup> (Fig. 4d). We raised a polyclonal antibody against GARRE and demonstrated that Flag-RAC1<sup>G12V</sup> precipitates endogenous GARRE (Fig. 4e). Knockdown of *GARRE* using short interfering RNA (siRNA) abrogated the GARRE signal in the Flag-RAC1<sup>G12V</sup> precipitate, thus confirming the specificity of our antibody (Fig. 4e). RAC1<sup>G12V</sup> and GARRE directly interacted, as demonstrated using immobilized recombinant His-RAC1<sup>G12V</sup> and purified GST-GARRE<sup>120–600</sup> (Fig. 4g). Deletion of amino acids 240–480 in GARRE (GARRE<sup>Δ240–480</sup>) abolished binding to GST-RAC1<sup>G12V</sup> (Fig. 4f).

#### Fig. 4: GARRE is a direct interactor of RAC1.



**a**, Dotplot showing BiOID interactions of KIAA0355 (named GARRE here) with Rac subfamily GTPases compared with Rho (ROCK2) or RAC1–CDC42 (PAK2) interactors. Bayesian FDR (BFDR) values are based on a SAINT analysis of  $n = 21,713$  interactions from indicated HEK293 samples, from which 4,609 interactions showed high confidence. A BFDR of 1% was applied as the threshold. **b**, Schematic of GARRE constructs used in this figure. See Extended Data Fig. 4b for details about the predicted amphiphysin-related BAR domain. **c**, Live-cell imaging of GFP-GARRE in HeLa cells. Red and yellow arrowheads point to GARRE accumulation in structures reminiscent of granules and tubular membranes. The broken line indicates the cell outline. Scale bar, 10  $\mu\text{m}$ . **d**, Western blots show the co-immunoprecipitation of Myc-GARRE with Flag-RAC1<sup>G12V</sup>, but not with Flag-RAC1<sup>WT</sup>, from Flp-In T-REx HEK293 lysates. **e**, Western blots show the co-immunoprecipitation of endogenous GARRE with Flag-RAC1<sup>G12V</sup> from HeLa lysates; the GARRE signal is absent following siRNA depletion of GARRE. **f**, Lysates of Flp-In T-REx HeLa cells expressing Flag-GARRE or Flag- GARRE<sup>A240–480</sup> were incubated with purified GST or GST-RAC1<sup>G12V</sup>. **g**, In vitro binding assays were performed using purified 6 $\times$ His-RAC1 and GST-GARRE<sup>120–600</sup>. GST and GST-PAK1<sup>67–150</sup> were used as negative and positive controls, respectively. **h**, Schematic of GARRE-TagRFP and the optogenetic probe PA-RAC1. In the dark, the LOV-Ja domains fused to RAC1<sup>Q61L</sup> masks its effector-binding domain. After excitation (blue light; 488 nm), a conformational change exposes RAC1<sup>Q61L</sup> for signalling. **i**, In PA-RAC1-expressing cells, repeated local illumination with blue light (cyan broken circle) induces relocalization of GARRE-TagRFP (lower panels; Supplementary Video 2) but not TagRFP (upper panels; Supplementary Video 1). The arrow indicates the membrane protrusion induced by PA-RAC1 activation. Scale bar, 10  $\mu\text{m}$  (applies to all images). **j**, The MFI ratio at the activated area was measured every 10 s for 100 s before blue light illumination (grey zone, light off) and for 500 s after repeated local illumination (white zone, light on). Data represent the mean  $\pm$  s.d. of  $n = 16$  TagRFP control cells and  $n = 13$  GARRE-TagRFP-expressing cells from two independent experiments. Data presented in this figure are representative of three independent experiments and are related to Unprocessed Blots Fig. 4.

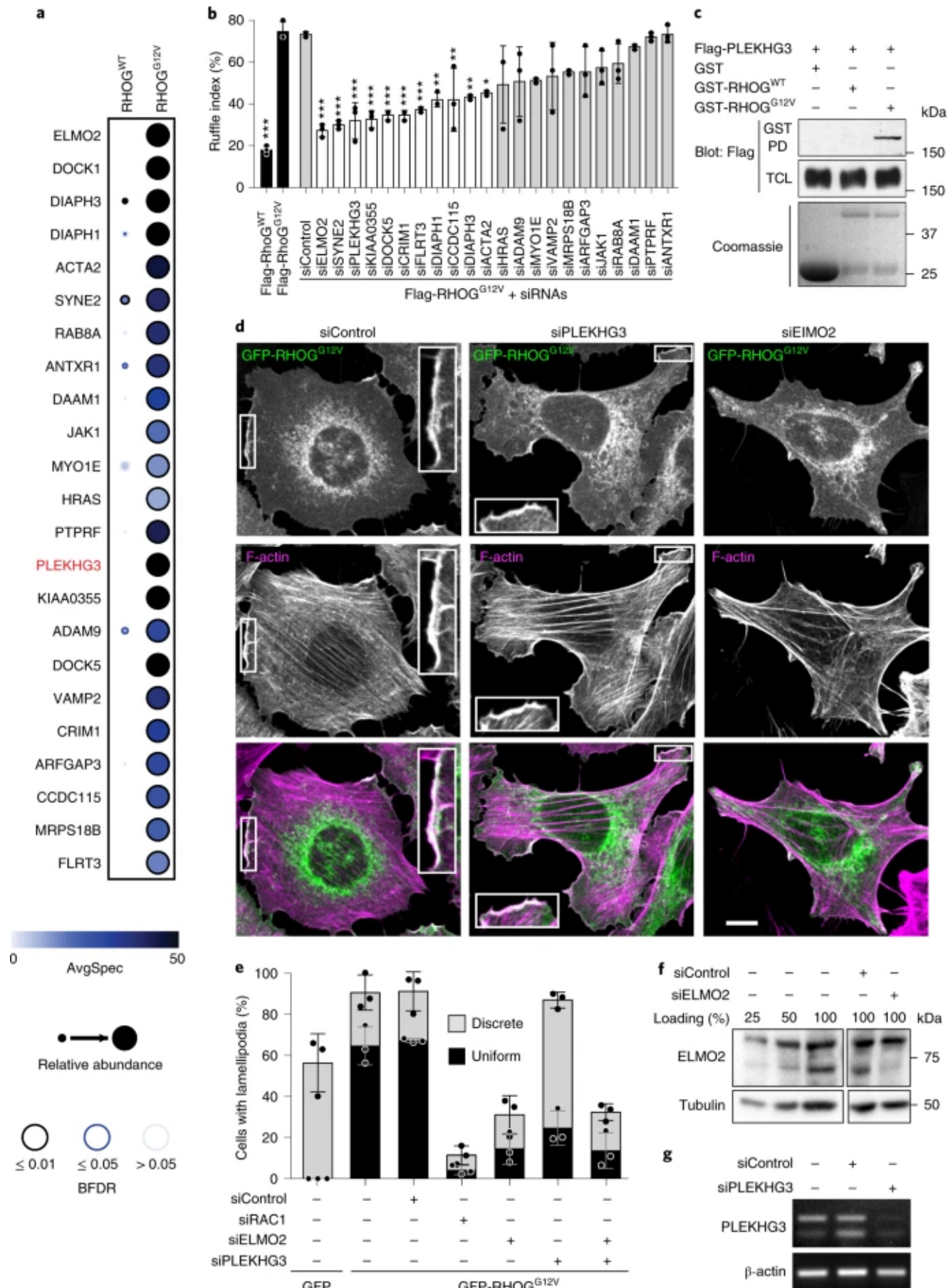
## Source data

Owing to its recovery with constitutive forms, we hypothesized that GARRE is a Rac family effector protein or a GAP. We ruled out that GARRE contains GAP activity (Extended Data Fig. 4d). We reasoned that if GARRE is an interactor of RAC1, local activation of RAC1 should promote its specific recruitment. We used optogenetics to address this by exploiting a genetically engineered photoactivatable form of RAC1

(PA-RAC1)<sup>64</sup> (Fig. 4h). Local excitation of PA-RAC1 in cells transfected with TagRFP induced the formation of lamellipodia adjacent to the excitation zone (Fig. 4i; Supplementary Video 1). We generated a TagRFP-GARRE protein to investigate whether local photoactivation of RAC1 promotes GARRE recruitment. TagRFP-GARRE was partially localized to discrete granules at  $t = 0$ , and following photoactivation of RAC1, its recruitment specifically to the region where PA-RAC1 was photoactivated was observable (Fig. 4i; Supplementary Video 2). This recruitment was often associated with an accumulation of GARRE in dynamic tubular-like structures (Supplementary Video 2, yellow arrow). The localization of TagRFP alone remained unchanged following photoactivation of PA-RAC1 (Fig. 4j). These data demonstrate that GARRE is an effector of RAC1.

PLEKHG3 is an effector of RHOG promoting Rac-mediated membrane ruffling. RHOG is the poorest characterized Rac subfamily member. To identify functional effectors of RHOG, we conducted a secondary screen by depleting 22 out of the 23 top proximal interactors (DOCK1 was omitted) by siRNA in cells expressing Flag-RHOG<sup>G12V</sup> and we quantified membrane ruffles via a high-content microscopy approach (Fig. 5a; Extended Data Fig. 5a). The proximal interactions of these candidates were increased with RHOG<sup>G12V</sup> in comparison to RHOG<sup>WT</sup> (Fig. 5a). Depletion of half the candidates, including ELMO2 (ref. 61), decreased RHOG<sup>G12V</sup>-induced membrane ruffling (Fig. 5b).

### Fig. 5: The GEF PLEKHG3 is an effector of RHOG.



**a**, Dotplot showing the top Bioid interactors of RHOG<sup>G12V</sup>. The BFDR is based on a SAINT analysis with  $n = 2,160$  interactions from the indicated HEK293 samples, from which 877 interactions showed high confidence (a BFDR of 1% was applied as the threshold). **b**, A functional siRNA screen for the 22 top interactors of RHOG<sup>G12V</sup> revealed potential effectors

promoting membrane ruffling (see Extended Data Fig. 5a for details). The percentage of cells presenting membrane ruffling was quantified on fixed cells stained with anti-Flag (Flag-RHOG<sup>G12V</sup>) and Alexa Fluor phalloidin (F-actin). Black bars represent untreated controls while white and grey bars represent the candidates presenting a significant or not phenotype, respectively. Data represent the mean  $\pm$  s.d. from  $n = 3$  independent experiments (90 cells per conditions).  $P$  values were calculated by one-way ANOVA, followed by Bonferroni's test; \* $P \leq 0.05$ , \*\* $P \leq 0.01$  and \*\*\* $P \leq 0.001$ . **c**, GST pulldown assays were performed on lysates from Flp-In T-REx HeLa cells expressing Flag-PLEKHG3 incubated with the indicated purified GST fusion proteins. Data are representative of three independent experiments. **d**, Confocal images show that the uniform membrane ruffle induced by RHOG<sup>G12V</sup> is reduced to multiple discrete membrane ruffles or no membrane ruffles after treatment with PLEKHG3 siRNA (siPLEKHG3) or ELMO2 siRNA (siELMO2), respectively. The inset enlargements show the overlay of GFP-RHOG<sup>G12V</sup> and F-actin staining in ruffles. Data are representative of three independent experiments. Scale bar, 10  $\mu$ m (applicable to all images). **e**, Graph shows the percentage of cells presenting uniform membrane ruffles versus multiple discrete ruffles for the indicated condition. Data represent the mean  $\pm$  s.d. from  $n = 3$  independent experiments (500 cells for control, 329 for RHOG<sup>G12V</sup>, 362 for siControl, 550 for siRAC1, 476 for siELMO2, 383 for siPLEKHG3 and 417 for siPLEKHG3 + ELMO2). **f**, Western blot shows ELMO2 depletion after 72 h of treatment with the indicated siRNAs. Tubulin was used as the loading control. Data are representative of two independent experiments. **g**, Expression levels of PLEKHG3 after 72 h of treatment with the indicated siRNAs were measured by semi-quantitative PCR with reverse transcription, with  $\beta$ -actin used as the control. Data are representative of two independent experiments. This figure is related to Unprocessed Blots Fig. 5.

### [Source data](#)

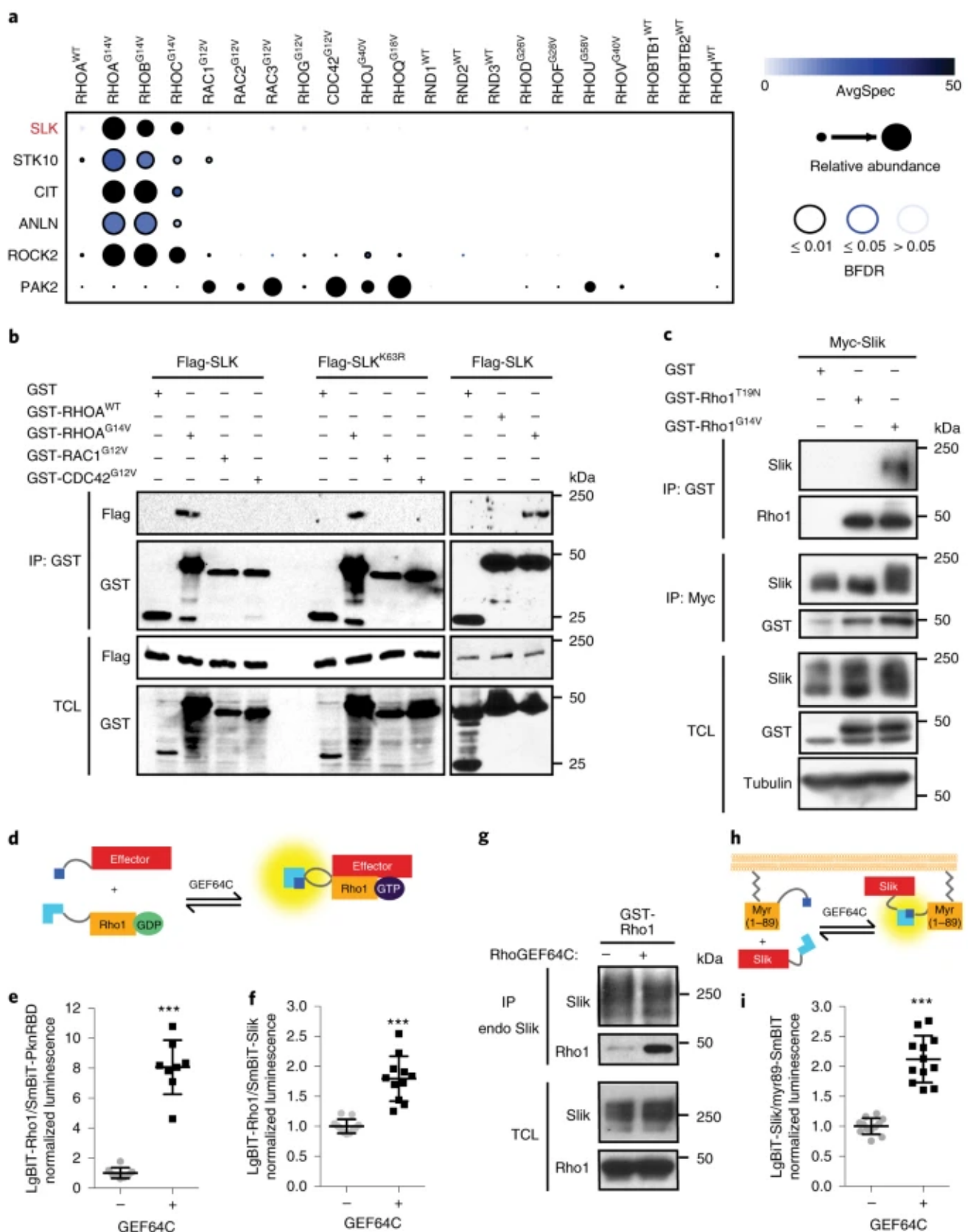
Among the uncharacterized RHOG candidate effectors, PLEKHG3 is a RAC1–CDC42 (ref. 51) and RHOA GEF (Fig. 2b). We investigated whether PLEKHG3 may act as an effector of RHOG to promote a GTPase-cascade controlling cytoskeleton reorganization. Pulldown assays confirmed that GST-RHOG<sup>G12V</sup> specifically bound to Flag-PLEKHG3 (Fig. 5c). This interaction is reminiscent of RHOG promoting RAC1 activation via ELMO–DOCK1 (ref. 61). We conducted siRNA depletion experiments to determine the respective contribution of ELMO–DOCK1 and PLEKHG3 to RHOG-induced cytoskeletal changes. The expression of eGFP-RHOG<sup>G12V</sup> stimulated lamellipodia formation, as more than 60% of cells expressing eGFP-RHOG<sup>G12V</sup>

displayed a large and uniform ruffle that we term ‘uniform’, while another 20% of cells displayed multiple ‘discrete’ protrusions that were also observed in about 50% of control cells expressing eGFP or eGFP-RHO $G^{WT}$  (Fig. 5d (first column) and 5e). Cell-shape computational analyses revealed that expression of eGFP-RHO $G^{G12V}$  was associated with a significant increase of cell circularity (mean value of 0.38 in control versus 0.73 after RHO $G^{G12V}$  expression, whereby a circularity value of 1.0 is a perfect circle) as cells become rounder (Extended Data Fig. 5c). Depletion of RAC1 decreased the presence of uniform and discrete protrusions (Fig. 5e; Extended Data Fig. 5b), decreasing the circularity back to control values (Extended Data Fig. 5d) and suggesting that signalling by RAC1 is central downstream of RHO. Depletion of PLEKHG3 decreased the circularity of the cells to the same level as RAC1 and abolished the formation of RHO $G^{G12V}$ -induced uniform ruffles (Fig. 5e; Extended Data Fig. 5d). However, residual discrete membrane protrusions were observed, which suggests that there is persistent local RAC1 activation that is PLEKHG3-independent (Fig. 5d,e,g). Depletion of ELMO2, or co-depletion of ELMO2 and PLEKHG3, revealed phenotypes similar to depletion of RAC1, whereby both uniform and discrete protrusions as well as circularity are decreased downstream of active RHO (Fig. 5d-f; Extended Data Fig. 5d). Coupling the discovery power of BioID to functional secondary screens is therefore a powerful approach to identify functional Rho-family effectors.

SLK is an effector of the RHOA subfamily mediating ERM proteins phosphorylation. The STE20 family of kinases SLK and STK10 (also known as LOK) interacted specifically with RHOA subfamily members, as indicated by high RSS values, similar to the known effectors CIT, ANLN and ROCK2 (Fig. 6a). The SLK proximal interaction with RHOA was enriched with the constitutively active mutant in comparison to the WT bait (Fig. 6a). We validated the BioID data by co-immunoprecipitation and revealed that GST-RHOA $G^{G14V}$  specifically bound to WT and kinase-dead forms of Flag-SLK (Fig. 6b). This interaction is evolutionarily conserved, as *Drosophila* GST-Rho1 $G^{G14V}$  specifically bound Myc-Slik (Fig. 6c). We developed biosensors to analyse the Slik and Rho1 interaction in live cells, whereby Rho1 GTP-loading status is manipulated by the co-expression of RhoGEF64C<sup>65</sup>. A split luciferase NanoBiT system

was used to monitor protein–protein interactions between Slik and the Pkn Rho-binding domain (positive control) tagged with Small BiT (SmBiT-Slik and SmBiT-Pkn-RBD, respectively) and Rho1 with Large BiT (LgBiT-Rho1) (Fig. 6d). The expression of RhoGEF64C increased the luciferase activity, which suggests that there was complex formation between SmBiT-Pkn-RBD and LgBiT-Rho1 (Fig. 6e). Co-expression of RhoGEF64C enhanced the coupling between LgBiT-Rho1 and SmBiT-Slik, as measured by an increase in luciferase activity over basal conditions (Fig. 6f). We observed a co-immunoprecipitation of GST-Rho1<sup>WT</sup> with endogenous Slik following expression of RhoGEF64C (Fig. 6g). We developed a biosensor strategy composed of a myristoylated-membrane-targeted SmBiT (Myr-SmBiT) and LgBiT-Slik to determine whether Rho1 activation induces the membrane recruitment of Slik (Fig. 6h). These experiments revealed that activation of Rho1 by RhoGEF64C promoted Slik targeting to membranes (Fig. 6i).

### Fig. 6: SLK binds RHOA in an evolutionarily conserved manner.



**a**, Dotplot showing the specificity of BiOID interactions of SLK and STK10 with RHOA<sup>G14V</sup> compared to RHOA (ROCK2, CIT and ANLN) or RAC1–CDC42 (PAK2) interactors. A BFDR 1% was applied, and the threshold is based on a SAINT analysis of 22,069 interactions from indicated HEK293 samples, from which 4,658 interactions showed high confidence. **b**, GST-pulldown assays in Flp-In T-REx HeLa cells expressing Flag-SLK or kinase-dead Flag-SLK<sup>K63R</sup> after transfection with indicated GST-fusion constructs. Data are representative of two

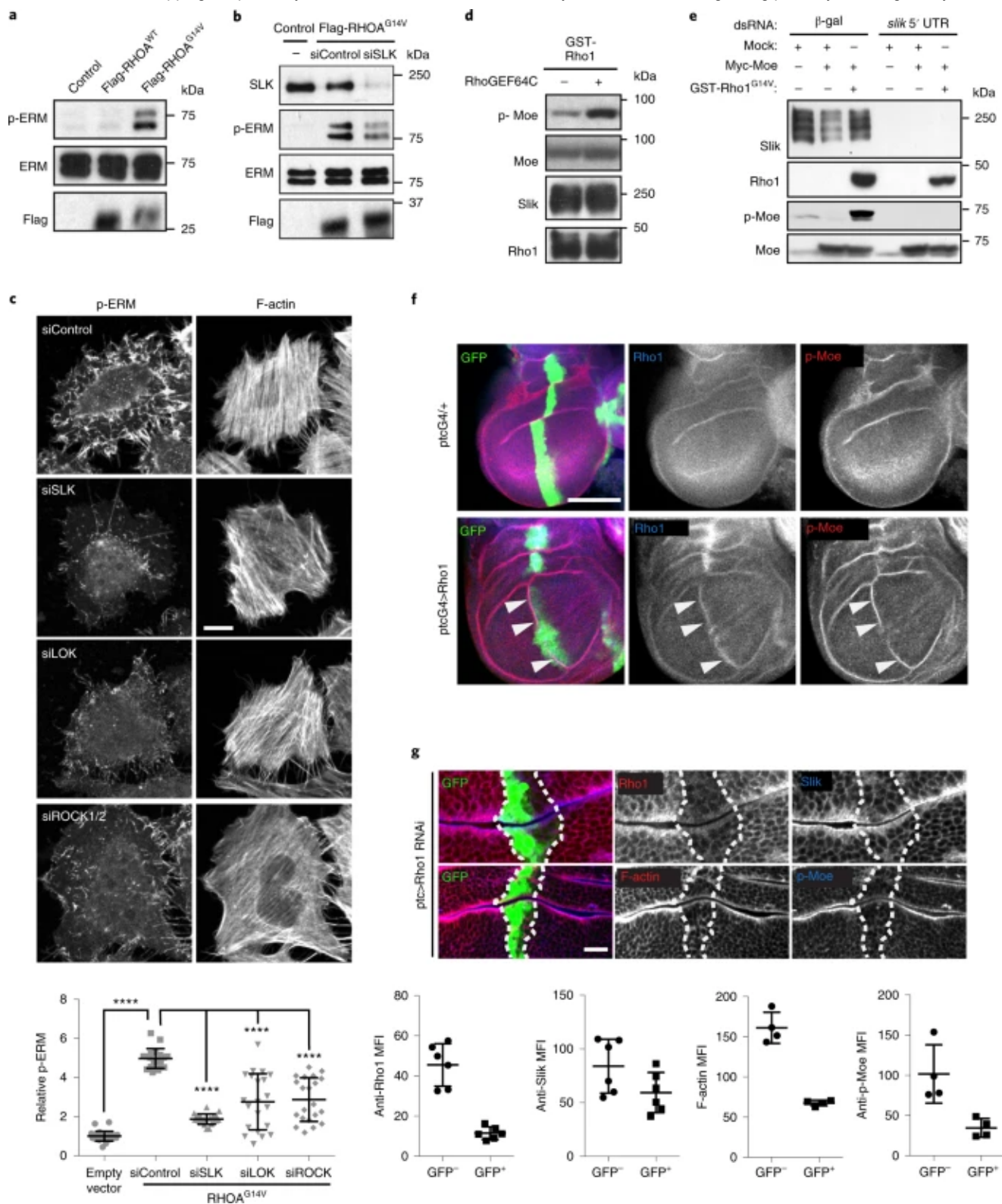
independent experiments. **c**, GST-pulldown and co-immunoprecipitation experiments performed in S2 cells co-expressing Myc-Slik with GST-Rho1<sup>G14V</sup> (constitutively active) or GST-Rho1<sup>T19N</sup> (inactive mutant). Data are representative of three independent experiments. **d**, Schematic representation of live-cell NanoBiT biosensor for Rho1 activity. Activation of Rho1 fused to LgBiT (light blue) leads to its interaction with the Rho-binding domain of Pkn tagged with the complementing SmBiT fragment (dark blue). **e**, NanoBiT complementation assay showing that RhoGEF64C activates Rho1, as evidenced by an increase in LgBiT-Rho1/SmBiT-PknRBD luciferase activity in S2 cells. Graph represents data from two experiments performed in quadruplicate ( $n = 8$ ). Control: normalized mean (s.d.) = 1.0 (0.332); GEF64C: normalized mean = 8.06 (1.68); two-sided  $t$ -test: \*\*\* $P = 3.26 \times 10^{-8}$ . **f**, NanoBiT complementation assay showing that RhoGEF64C activation of Rho1 promotes its interaction with Slik, as evidenced by an increase in LgBiT-Rho1/SmBiT-Slik luciferase activity in S2 cells. Graph represents data from three experiments performed in triplicate or quadruplicate ( $n = 11$ ). Control: normalized mean (s.d.) = 1.0 (0.110); GEF64C: normalized mean = 1.79 (0.357); two-sided  $t$ -test: \*\*\* $P = 1.53 \times 10^{-6}$ . **g**, Co-immunoprecipitation experiment of S2 cells expressing GST-Rho1, with or without RhoGEF64C. Experiment was performed once. **h**, Schematic representation of a NanoBiT biosensor for Slik membrane recruitment based on a membrane-associated SmBiT fused to the myristoylated sequence of *Drosophila* Src. **i**, NanoBiT complementation assay showing that GEF64C activation of Rho1 stimulates an interaction of Slik with membranes, as evidenced by an increase in LgBiT-Slik/myr89-SmBiT luciferase activity in S2 cells. Graph represents data from three experiments performed in quadruplicate ( $n = 12$ ). Control: normalized mean (s.d.) = 1.0 (0.128); GEF64C: normalized mean (s.d.) = 2.12 (0.376); two-sided  $t$ -test: \*\*\* $P = 3.96 \times 10^{-9}$ . This figure is related to Unprocessed Blots Fig. 6.

#### Source data

SLK phosphorylates ERM proteins to promote their conformational activation in mammalian cells and *Drosophila*<sup>66,67</sup>. RHOA<sup>G14V</sup> was shown to specifically promote the phosphorylation of ERMs at their regulatory site, but the mechanism behind this regulation has remained unresolved for two decades<sup>68</sup>. We hypothesized that RHOA family members may recruit SLK/Slik to membranes to control their kinase activity to mediate ERM phosphorylation. We confirmed that the expression of Flag-RHOA<sup>G14V</sup> specifically induced the phosphorylation of ERM proteins (Fig. 7a). We found that the depletion of SLK and LOK by siRNAs diminished Flag-RHOA<sup>G14V</sup>-induced ERM

phosphorylation (Fig. 7b,c; Extended Data Fig. 6a). Additional kinases besides SLK are candidate ERM kinases, including ROCK1 and ROCK2 (ref. 69). The depletion or pharmacological inhibition of ROCK1 and ROCK2 led to a decrease in RHOA<sup>G14V</sup>-induced phosphorylation of ERMs (Fig. 7c; Extended Data Fig. 6). The RHOA-induced phosphorylation of ERMs was conserved in *Drosophila*, as expression of GST-Rho1<sup>G14V</sup> promoted the phosphorylation of the only ERM protein in flies (Moesin (Moe)) in a Slik-dependent manner (Fig. 7d,e). To test whether Rho1 can promote Moe phosphorylation in vivo, we expressed GFP alone or together with Rho1 using the *patched-Gal4* driver (*ptcG4*), which leads to protein expression in a central stripe of cells in the developing fly wing imaginal disc. These experiments revealed that the expression of Rho1 forced ectopic phosphorylated Moe (p-Moe) specifically in the *ptc* stripe (see arrows in Fig. 7f). Conversely, partial siRNA-mediated depletion of *Rho1* in vivo in the *ptc* stripe was sufficient to delocalize Slik from the apical membrane and decrease apical p-Moe and polymerized actin (Fig. 7g).

**Fig. 7: SLK induces RHOA-dependent phosphorylation of ERM proteins.**



**a**, Western blot showing ERM proteins phosphorylation (p-ERM) in the presence of Flag-RHOA<sup>G14V</sup> or Flag-RHOA<sup>WT</sup>. Data are representative of three independent experiments. **b**, Induction of p-ERM by RHOA<sup>G14V</sup> is decreased by siRNA-mediated SLK depletion. Data are representative of four independent experiments. **c**, Upper: confocal images of RHOA<sup>G14V</sup>-expressing cells treated with indicated siRNAs and stained for p-ERM and F-actin. Images are representative of three independent experiments. Scale bar, 10  $\mu$ m (applicable to all images). Lower: graph shows relative p-ERM MFI  $\pm$  s.d. in RHOA<sup>G14V</sup>-expressing cells treated with indicated siRNAs compared to untransfected cells ( $n = 25$  images for empty vector,  $n = 18$  for siControl,  $n = 18$  for siSLK,  $n = 18$  for siLOK,  $n = 18$  for siROCK).

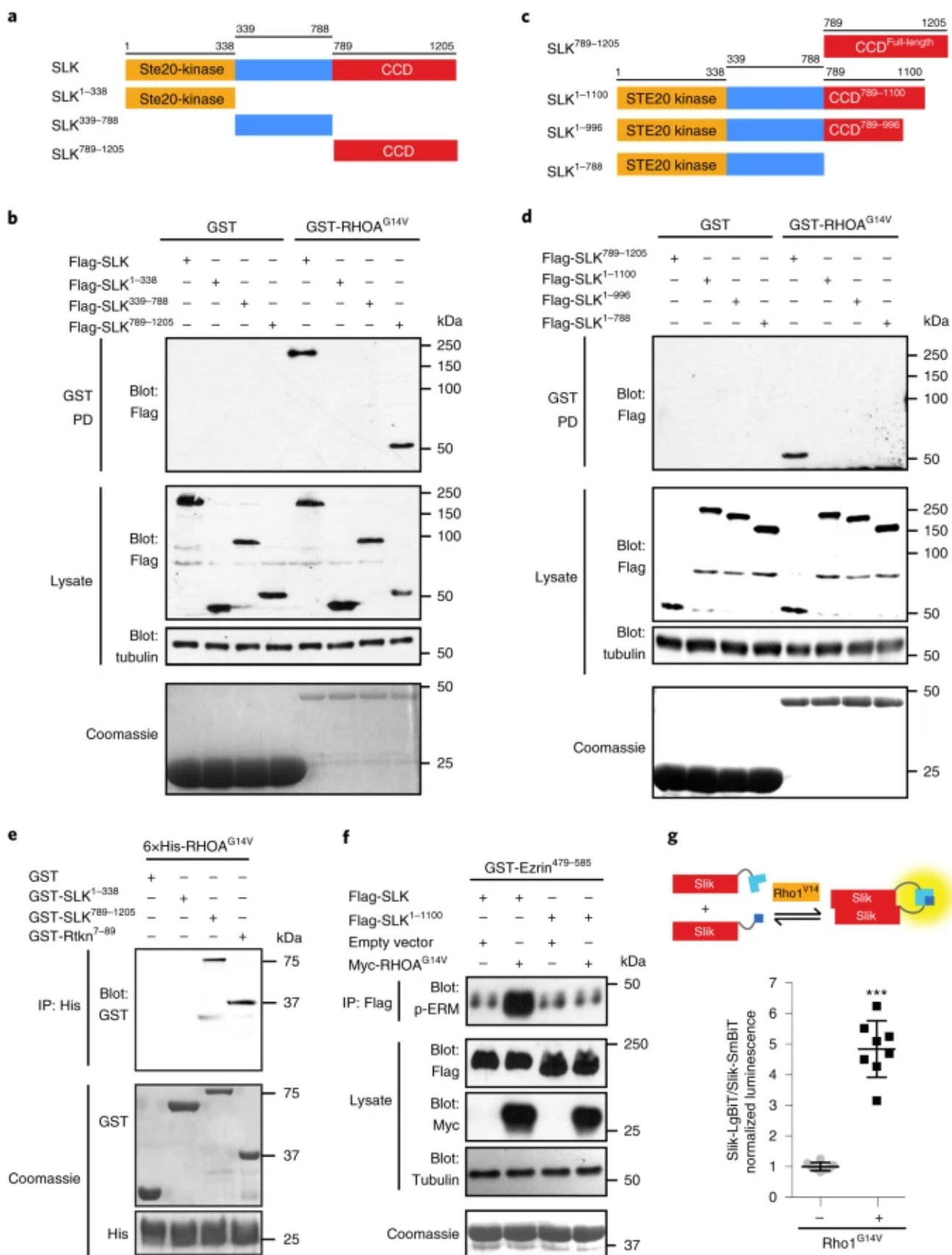
siControl, 20 for the other siRNAs; two independent experiments). *P* values were calculated using Mann–Whitney nonparametric two-tailed tests; \*\*\*\**P* < 0.0001. **d**, GST pulldown experiment in S2 cells expressing GST-Rho1, with or without RhoGEF64C. Experiment was performed once. **e**, S2 cells were treated with dsRNA targeting β-galactosidase or *slik* to deplete Slik, and then mock-treated or induced to express Myc-Moe in the presence or absence of GST-Rho1<sup>G14V</sup>. Data are representative of two independent experiments. **f**, Confocal micrographs of *Drosophila* wing imaginal discs expressing GFP alone (upper) or together with Rho1 (lower) in a central stripe of cells under the control of the *ptc*-GAL4 driver, and immunostained for Rho1 (red) and p-Moe (blue). Rho1 misexpression causes ectopic p-Moe in the *ptc* domain (arrowheads). Scale bar, 100 μm (applicable to all images). Data are representative of two independent experiments. **g**, Upper: confocal micrographs of wing imaginal discs expressing a dsRNA targeting *rho*1 under the control of *ptc*-GAL4, marked by co-expression of GFP. Images are taken at a fold in the disc, where two surfaces of the epithelial layer abut their apical membranes apposed. Endogenous Rho1 (red) and Silk (blue) (upper), or F-actin (red, phalloidin) and p-Moe (blue) (lower) were stained. Broken lines indicate limits of the GFP<sup>+</sup> *ptc* expression domain. Scale bar, 10 μm (applicable to all images). Lower: graphs show MFI ± s.d. from apical Rho1, Slik, F-actin and p-Moe staining measured in *rho*1-depleted GFP<sup>+</sup> cells versus neighbouring WT GFP<sup>−</sup> cells on each side of the fold. *n* = 6 (Rho1, Slik) or *n* = 4 (p-Moe, F-actin) from three or two independent animals. This figure is related to Unprocessed Blots Fig. [7](#).

### [Source data](#)

We investigated whether SLK is directly activated by RHOA. SLK is composed of an N-terminal kinase domain, a central linker region and a C-terminal coiled-coil domain (CCD)[70](#). We generated these domains as GST-fused proteins to map the region on SLK that interacts with Flag-RHOA<sup>G14V</sup> and revealed that the CCD is responsible for this function (Fig. [8a,b](#)). We truncated the CCD to identify the minimal binding region and found that a deletion of the last 105 residues was sufficient to abolish Flag-RHOA<sup>G14V</sup> binding (SLK<sup>1–1100</sup>; Fig. [8c,d](#)). We confirmed that this interaction is direct via co-immunoprecipitation using purified His-RHOA<sup>G14V</sup> and GST-CCD proteins (Fig. [8e](#)). To determine whether the CCD is important in mediating SLK activation by RHOA, we expressed Flag-SLK<sup>WT</sup> or Flag-SLK<sup>1–1100</sup>, alone or together with Myc-RHOA<sup>G14V</sup>, and carried out in vitro kinase assays to measure SLK kinase activity. RHOA<sup>G14V</sup> increased the kinase activity of SLK<sup>WT</sup> while it failed to stimulate the

activity of SLK<sup>1–1100</sup> (Fig. 8f). We found that Rho1<sup>G14V</sup> promoted the dimerization of Slik in a live-cell biosensor assay, which suggests that this is a possible mechanism of activating this kinase (Fig. 8g). In summary, SLK is activated by RHOA in an evolutionarily conserved manner to promote the phosphorylation of ERMs.

**Fig. 8: RHOA<sup>G14V</sup> directly binds the C-terminal CCD of SLK.**



**a**, Schematics of the SLK domain constructs: kinase domain (SLK<sup>1-338</sup>; yellow), linker domain (SLK<sup>339-788</sup>; blue) and CCD (SLK<sup>789-1205</sup>; red). **b**, GST pulldown assays performed using lysates from Flp-In T-REx HeLa cells expressing SLK full-length or the indicated SLK domains incubated with purified GST or GST-RHOA<sup>G14V</sup>. Tubulin was used as the loading control. Coomassie-stained gel of purified GST and GST-RHOA<sup>G14V</sup>. Data are representative of three

independent experiments. **c**, Schematic representation of the SLK CCD truncations. **d**, GST pulldown assays were performed using lysates from Flp-In T-REx HeLa cells expressing the SLK CCD or the indicated SLK CCD truncations incubated with purified GST or GST-RHOA<sup>G14V</sup>. Tubulin was used as the loading control. Coomassie-stained gel of purified GST and GST-RHOA<sup>G14V</sup>. Data are representative of three independent experiments. **e**, Purified CCD of SLK (GST-SLK<sup>789–1205</sup>) co-immunoprecipitation with purified 6×His-RHOA<sup>G14V</sup> but not the kinase domain (GST-SLK<sup>1–338</sup>). The Rho-binding domain of murine Rhotekin (GST-Rtnk<sup>7–89</sup>) was used as a positive control. Data are representative of four independent experiments. **f**, Lysates from HeLa cells expressing Flag-SLK or the RHOA-binding-deficient truncation Flag-SLK<sup>1–1100</sup> alone or with RHOA<sup>G14V</sup> were incubated with purified GST-Ezrin<sup>479–585</sup> and an in vitro kinase assay was performed. Ezrin phosphorylation was detected using anti-p-ERM antibody. Tubulin was used as the loading control. Coomassie-stained gel shows the total amount of GST-Ezrin<sup>479–585</sup> in the kinase assay. **g**, Schematic representation of a live-cell NanoBiT biosensor for measuring Slik dimerization, using C-terminally LgBiT and SmBiT-tagged forms of Slik. NanoBiT complementation assay with this biosensor indicates that activated Rho1<sup>G14V</sup> promotes Slik C terminus dimerization in S2 cells. Graph represents compiled data from two experiments performed in quadruplicate ( $n = 8$ ). Control: normalized mean (s.d.) = 1.0 (0.127); Rho1<sup>G14V</sup>: normalized mean (s.d.) = 4.84 (0.8620); two-sided *t*-test: \*\*\* $P = 1.36 \times 10^{-8}$ . This figure is related to Unprocessed Blots Fig. 8.

#### [Source data](#)

## Discussion

The Ras family of proteins transmit their signals by engaging in protein–protein interactions with multiple GEFs, GAPs and effectors, and large-scale methods are needed to define the organization of these signalling hubs. Here, we systematically defined the Rho family interaction network by revealing their proximity interacting protein profiles in various nucleotide-loading states. The large number of interactions recovered by BiOID has not been achievable with traditional approaches to studying Rho proteins. The strength of the BiOID approach is to monitor proximity, transient and stable interactions between Rho proteins and their target protein complexes while they are taking place in specialized membranous microenvironments in cells. These approaches should be applicable to all Ras GTPases, and small-scale evidence supports this theory<sup>71</sup>. Our data demonstrate the reliability of BiOID applied to Rho proteins as it confirmed activity-dependent

established interactions. A long-standing challenge has been to define the GEFs and GAPs globally controlling the activity of individual Rho proteins in cell-type specific contexts. In agreement with previous findings<sup>12,52</sup>, we demonstrated that some GEFs are selective for individual Rho proteins whereas GAPs are promiscuous. From a practical standpoint, similar profiling experiments can be carried out in any cell type, such that it should be a powerful approach to identify candidate GEFs and GAPs of a Rho protein and probe their functional relevance by genetic approaches (for example, via siRNA or CRISPR (clustered regularly interspaced short palindromic repeats)). One limitation could be that the mutations used to alter nucleotide loading create biases such as altered localization, which would produce a certain number of false-positive proximal interactions. It remains important to experimentally validate the proximal interactions of interest in functional assays.

An objective of this study was to define the Rho family effector landscape. We defined the effector proteins that preferentially interact with the different Rho subfamily of proteins. GARRE was such a candidate effector specific to the Rac subfamily of proteins. GARRE displays unique localization features, and future studies are needed to resolve its functions. Likewise, we uncovered a specific interaction between RHOA subfamily proteins and SLK that opened the door to revisit a two-decade-old roadblock in the field. We demonstrated that the RHOA interaction with SLK is evolutionarily conserved and we mapped the CCD of SLK in mediating this interaction. Other effectors (for example, ROCK1 and CIT) use coiled-coil motifs to bind RHOA<sup>72</sup>. Our work is consistent with a model whereby SLK is autoinhibited via intramolecular contacts, since binding of the CCD to RHOA stimulates its kinase activity.

A previous study<sup>72</sup> published the most complete Rho interactome to date by incubating six bacterially purified GTPγS-loaded Rho proteins with cell extracts. The approach used in that study revealed a high level of promiscuity since Rho GTPases displayed binding to many effectors, as exemplified by ROCK1 binding to almost all baits. Our BioID approach yielded more specific results for interactions between different Rho subfamily proteins and target proteins. GARRE, a RAC1 interactor identified by BioID, was not biochemically detected<sup>72</sup>. Re-analyses of RHOA–RHOC

pulldowns in that study<sup>72</sup> revealed that SLK bound to RHOA but not RHOB or RHOC. Hence, BioID identified an additional layer of interactions occurring in cells. We began to characterize proximity interactors, but the majority of the data remain to be explored to uncover unexplored functions of Rho proteins. We make our BioID data available on a dedicated website ([http://prohits-web.lunenfeld.ca/GIPR/Datasets.php?projectId=25&m\\_num=m3](http://prohits-web.lunenfeld.ca/GIPR/Datasets.php?projectId=25&m_num=m3)) to assist the research community in exploring Rho interactions.

## Methods

---

Antibodies, siRNAs, plasmids and primers

Antibodies and cell-staining reagents are listed in Supplementary Table 2, siRNAs in Supplementary Table 3, plasmids in Supplementary Table 4 and primers in Supplementary Table 5. The gateway-compatible complementary DNA library of Rho genes has been previously described<sup>73</sup>.

Cell culture, generation of stable cell lines and siRNA transfections

Cells were maintained at 37 °C in 5% CO<sub>2</sub> in DMEM supplemented with 10% fetal bovine serum (F1051, Sigma-Aldrich) and 1% penicillin–streptomycin (450-201-EL, Wisent). Stable Flp-In T-Rex HEK293 (Thermo Fisher) or Flp-In T-Rex HeLa cell lines (gifts from S. Taylor, University of Manchester, UK) expressing BirA\*-Flag-RHOs or other constructs were generated as recommended by manufacturers, and protein expression was induced with tetracycline (1 µg ml<sup>-1</sup>; 24 h). For BioID, cells were cotreated with 50 µM biotin and tetracycline. siRNA transfections were performed using 50 nM of siRNA using Lipofectamine 2000 (12566014, Invitrogen) according to the manufacturer's recommendations.

BioID purification and MS

BioID experiments were performed as previously described<sup>19,74</sup>. Briefly, cleared lysates were incubated with 70 µl of streptavidin beads (5 ml; 17-5113-01, GE Healthcare) at 4° for 3 h, washed with lysis buffer followed by washes in 50 mM ammonium bicarbonate (AB0032, 500G, Biobasic). For trypsin digestion, 1 µg of trypsin (T6567, Sigma-Aldrich) was added into each 100 µl sample in 50 mM

ammonium bicarbonate overnight, followed by an additional 1 µg of trypsin for an extra 2 h. Supernatants were transferred into new microtubes, beads were washed two times with 100 µl of water and supernatants from all washes were pooled with the initial supernatant. Formic acid (5%, 250 ml; 94318, Sigma-Aldrich) was added into each tube and supernatants were transferred into new microtubes and dried in a SpeedVac. Pellets were resuspended in 15 µl of 5% formic acid and kept at –80 °C. Samples originating from Flp-In T-REx HEK293 cell lines and Flp-In T-REx HeLa cell lines were injected into LTQ-Orbitrap Velos and Q Exactive mass spectrometers (Thermo Fisher), respectively. Tryptic peptides were loaded onto a 75-µm internal diameter × 150 mm Self-Pack C18 column installed in an Easy-nLC 1000 system (Proxeon Biosystems). Buffers used for chromatography were 0.2% formic acid (buffer A) and 90% acetonitrile/0.2% formic acid (buffer B). Peptides were eluted with a two-slope gradient at a flow rate of 250 nl min<sup>-1</sup>. Solvent B first increased from 2% to 35% in 100 min and then from 35 to 80% in 10 min. On both instruments, the high-performance liquid chromatography system was coupled to a Nanospray Flex Ion Source. Full-scan MS survey spectra (*m/z* 360–2,000) in profile mode were acquired in the Orbitrap with a resolution of 60,000. Collision-induced dissociation and higher-energy collisional dissociation fragmentation modes were used for samples injected in LTQ Orbitrap Velos and Q Exactive mass spectrometers, respectively. The 15 most intense peptide ions were fragmented in the collision cell and MS/MS spectra were analysed in the linear ion trap (LTQ Orbitrap Velos) or in the Orbitrap (Q Exactive). Results were acquired throughout the experiments at different times to mitigate against batch effects.

## MS data analyses

Raw MS files were analysed using the Mascot search engine through the iProphet pipeline integrated in Prohits<sup>75</sup> and the Human RefSeq database (v.57) supplemented with “common contaminants” from the Max Planck Institute (<http://maxquant.org/downloads.htm>), the Global Proteome Machine (<http://www.thegpm.org/crap/index.html>) and decoy sequences. Mascot parameters were set with trypsin specificity (two missed cleavage allowed) and Oxidation (M) and Deamidation (NQ) as variable modifications. Mass tolerances for precursor and

fragment ions were set to 15 ppm and 0.6 Da, respectively, and peptide charges of +2, +3 and +4 were considered. Resulting Mascot search results were individually processed using PeptideProphet, and peptides were assembled into proteins using parsimony rules first described in ProteinProphet using the Trans-Proteomic Pipeline with the following parameters: -p 0.05 -x20 -PPM – “DECOY”; iProphet options: pPRIME; and PeptideProphet: pP. Sample reproducibility was assessed using Perseus by graphing raw spectral counts of each biological replicate in a multiscatter plot and by calculating Pearson’s correlation values. Biological replicates below a Pearson’s correlation value of 0.9 were discarded and reacquired.

### Interaction scoring

To estimate interaction statistics, we used SAINTexpress<sup>76</sup> (v.3.6.1) on proteins with an iProphet protein probability of  $\geq 0.9$  and unique peptides  $\geq 2$ . Each proteomics dataset (Rho constitutively active, nucleotide-free and WT forms, each expressed in HEK293 and HeLa cells) was compared separately against their respective negative controls. These controls comprised pull-downs from both cell lines expressing empty vector or eGFP-BirA\*-Flag was each generated in four biological replicates. SAINT analyses were performed with the following settings: nControl:2, nCompressBaits:2 (negative controls compressed twofold to  $n$  virtual controls and no baits compression). From the SAINT analyses results, prey specificities (WD score) were calculated with CompPass from the ProHits-viz Prey Specificity online tool<sup>77</sup>. Interactions displaying an average probability (AvgP) of  $\geq 0.95$  were considered statistically significant and of high confidence (Supplementary Table 7 (HEK293 constitutively active), Supplementary Table 8 (HeLa constitutively active), Supplementary Table 9 (HEK293 nucleotide-free) and Supplementary Table 10 (HeLa nucleotide-free)). Supplementary Table 11 contains combined and filtered results of Supplementary Tables 7 and 8 (active baits). Supplementary Table 12 contains combined and filtered results of Supplementary Tables 9 and 10 (nucleotide-free baits). Unfiltered contaminants (for example, keratins and  $\beta$ -galactosidase) were manually removed. Complete lists of annotated and scored interactions are also available at ProHits.

## Bioinformatics analyses

All proteomics data and annotation databases (BioGRID (human v.3.4.164), UniProt (human release 2017-10), CORUM (v.3.0 release 03.09.2018), Gene Ontology Annotation Database (GOA) and Pfam (human v.32.0)) were imported into a MySQL database. Graphical representations of protein–protein networks were generated using Cytoscape (v.3.7.0), with WD scores as edge-weighted attributes. Network augmentations of BioID were performed by extracting prey–prey interactions from the human BioGRID network and from Cytoscape’s PSICQUIC Web Service client (October 2018 releases) searching IntAct, iRefIndex, Reactome, Mint and UniProt databases.

## Dotplot analyses

SAINT output files of BirA\*-Flag-RHO baits or controls analysed in ProHits were processed through ProHits-Viz to carry out dotplot analyses<sup>77,78</sup>. AvgP  $\geq 0.95$  or BFDR  $\geq 0.95$  cut-offs were used to report high-confidence interactions.

## Recall analyses

To identify top candidate Rho effectors from the BioID of active Rho baits datasets, we applied, in addition to the AvgP  $\geq 0.95$  from SAINT analyses, a combination of two additional filters: the preys’ AvgSpec, a proxy for relative abundance, and the preys’ CAAX ratio (Preys AvgSpec/CAAX AvgSpec), which displays the enrichment against a control in which a BirA\*-Flag-GFP fusion is targeted to membranes through a CAAX box. Selection of the cut-offs for these filters was established as previously described<sup>20</sup> by performing interaction recalls with the BioGRID database.

Interactions were sorted by decreasing the AvgSpec or CAAX ratio, and the number of recovered BioGRID interactions was counted by increasing bins of 500 interactions (Supplementary Tables [13](#) and [14](#) (AvgSpec) and Supplementary Tables [15](#) and [16](#) (CAAX ratio)). From this, we selected AvgSpec thresholds of 6.5 and 17, and CAAX ratio thresholds of 0.73 and 1.10 for the HEK293 and HeLa Rho constitutively active datasets, respectively.

## RHO RSS

By performing BiOID screens in two cell lines (HEK293 and HeLa), we aimed to uncover the most accurate Rho interactome by combining filtered interactions (see “Recall analyses” section) of both cell lines. This increases the confidence of shared interactions between the cell lines while keeping the ones that are unique from either cell line. We first pooled the interaction specificity scores from both cell lines by summing their respective WD score, generating a cells-combined WD score, followed by a  $\log_2$  transformation and rescaled on a range of 0.1 to 1.0 with the R Scales package. To identify top candidate Rho effectors, we took advantage of the Rho phylogenetic hierarchy by grouping the values into known Rho subfamilies<sup>11</sup>. For each subfamily, we first segregated prey into groups of  $n$ -level of subfamily promiscuity (number of proximity-interacting baits within each subfamily). Second, we sorted the values decreasingly by the RHO RSS, which integrates, for a given prey, the sum of its cells-combined WD scores within a given subfamily. From these sorted values, we generated heatmaps (without clustering) with the Pheatmap package in R ([www.r-project.org](http://www.r-project.org)).

Co-immunoprecipitations, GST pulldowns and in vitro kinase assays

Cells were lysed in CHAPS buffer (30 mM Tris-HCl, pH 7.5, 150 mM NaCl, 5 mM MgCl<sub>2</sub> and 1% CHAPS), and cleared lysates were incubated for 3 h at room temperature with glutathione beads (L00206-10ml, GenScript) or with Flag-M2 agarose (A2220, Sigma-Aldrich). For in vitro kinase assays, lysates of HeLa cells expressing the indicated SLK constructs were subjected to immunoprecipitation using Flag-M2 agarose. Beads were washed three times in CHAPS buffer, two times in 2× kinase reaction buffer (50 mM Tris-HCl, pH 7.5, 100 mM NaCl, 6 mM MgCl<sub>2</sub> and 1 mM MnCl<sub>2</sub>). Beads were incubated for 1 h at 30 °C with purified GST or GST-Ezrin<sup>479–585</sup> in 15 µl of kinase reaction buffer supplemented with 2 mM dithiothreitol, 50 µM ATP, 1 mM Na<sub>2</sub>VO<sub>4</sub>, 5 mM NaF, 2.5 mM sodium pyrophosphate and 1× PhosSTOP (04906845001, Roche). Phosphorylation and expression levels were analysed by immunoblotting or Coomassie staining.

## Protein purification and direct interaction assays

Expression of GST-tagged or 6×His-tagged proteins in BL21 bacteria was induced with 0.1 mM isopropyl-β-D-thiogalactoside for 3 h at 37 °C or overnight at 20 °C with shaking. The proteins were purified according to manufacturers' recommendations. Briefly, cleared lysates were incubated with glutathione-resin or His-select nickel affinity (P6611, Sigma-Aldrich) beads for 2 h at 4 °C with rotation. Samples were washed three times with PBS with Tween or lysis buffer. GST-tagged proteins on beads were eluted with elution buffer (50 mM Tris-HCl, pH 8.0, 10 mM glutathione), and buffer was exchanged to PBS using centrifugal filter units (UFC801024, EMD Millipore). Approximately 500–800 ng of collected GST-tagged proteins was allowed to interact with either 6×His-RHOA<sup>G14V</sup> or 6×His-RAC1<sup>G12V</sup> beads in CHAPS buffer for 3 h at 4 °C with rotation. Samples were denatured and subjected to SDS-PAGE. Purified GST-tagged or 6×His-tagged proteins levels and integrity were verified by Coomassie staining.

## High-content microscopy and imaging analysis

Indicated Flp-In T-REx HeLa lines were transfected for 2 days with a custom-designed set of siRNAs targeting BiOID candidates. Cells were plated on Cellbind surface 96-well plates (3340, Corning), and expression of RHOG proteins was induced with tetracycline. Cells were fixed and stained using anti-Flag M2 antibody and Alexa Fluor phalloidin as described below. Images were taken using a high-content microscope (ImageXpress, Molecular Devices) and analysed using MetaXpress (Molecular Devices) or ImageJ software. The percentage of ruffle index was quantified as described elsewhere<sup>79</sup> using the ADAPT plug-in for ImageJ. Briefly, membrane ruffles were identified by colocalization between Flag-RHOG<sup>G12V</sup> and the phalloidin signals at the cell periphery. Flag or phalloidin images in greyscale were opened in ADAPT and the following parameters were used. ImageJ's multipoint selector tool was used to select the cells in the phalloidin image. The phalloidin image was assigned for the cytoplasmic channel and the Flag image for the signal to be correlated. Auto Threshold (Huang method) and Generate Signal Distribution functions were selected. A value between 1.0 and 2.0 was set for the smoothing filter radius.

## Cell staining and confocal microscopy analyses

Indicated Flp-In T-REx HeLa cells were plated on coverslips overnight in the presence of  $1\text{ }\mu\text{g ml}^{-1}$  tetracycline before fixation. When mentioned,  $50\text{ }\mu\text{M}$  biotin was also added. For CP110 staining, cells were prefixed with 0.4% paraformaldehyde in PBS for 5 min at  $37\text{ }^\circ\text{C}$  and pre-extracted with 0.5% TritonX-100 in PHEM (50 mM PIPES buffer, 50 mM HEPES buffer, 10 mM EGTA, 10 mM MgCl<sub>2</sub>, pH 6.9) for 2 min at  $37\text{ }^\circ\text{C}$ . Extracted cells were washed with PBS and fixed with 4% paraformaldehyde in PBS for 5 min at room temperature followed by extraction in ice-cold methanol for 5 min. For every other staining, cells were fixed with 3.7% formaldehyde in CSK buffer (100 mM NaCl, 300 mM sucrose, 3 mM MgCl<sub>2</sub>, 10 mM PIPES, pH 6.8) for 15 min. Fixed cells were extracted in 0.2% Triton X-100 in PBS. Antibody dilutions and incubation times are detailed in Supplementary Table 2. Fixed cells were incubated with primary antibodies diluted in wash buffer (TBS supplemented with 1% BSA, 0.1% Triton-X100) followed by five washes before incubation with secondary antibody, together with phalloidin and/or streptavidin when mentioned. Cells were washed ten times followed by one wash with water before mounting coverslips in Mowiol. Images were collected on a Carl Zeiss LSM710 confocal laser scanning microscope (Carl Zeiss MicroImaging) equipped with a  $x-y-z$  motorized stage, a plan-apochromat  $\times 63/1.4$  numerical aperture objective, 4 laser lines for excitation (405, 488, 555 and 638 nm), driven by ZenBlack 2009 software. For p-ERM analyses, all acquisition parameters were maintained between conditions. Quantitative analyses of ERM protein phosphorylation were performed using Fiji (National Institutes of Health). A region of interest (ROI) was created using the threshold images of the F-actin channel. This ROI was transferred to the correspondent background-subtracted p-ERM images and the mean fluorescence intensity (MFI) was measured. The data were normalized using the negative control (HeLa cells without RHOA<sup>G14V</sup>) with an arbitrary MFI of 1. The normalized data were transferred to Prism 7 software (GraphPad Prism) for further analyses. Unbiased analysis of the cell circularity ( $4\pi(\text{area}/\text{perimeter}^2)$ ) was performed using the shape descriptor Plugin in Fiji for each individual cell expressing cycle3-GFP-RHOG<sup>G12V</sup> or GFP. A circularity value of 1.0 indicates a perfect circle. Relative frequency distribution was calculated using Prism 7 software using a Bin width of 0.1. The frequency distribution curves were created using Microsoft Excel.

The percentage of uniform versus discrete lamellipodia was determined by counting cells presenting the phenotype depicted in Fig. 5d using the same set of images.

#### Local optogenetic activation of PA-RAC1

HeLa cells were transfected with PA-RAC1 and TagRFP or GARRE-TagRFP using Lipofectamine 3000, and cells were plated on glass bottom dishes (MatTek Corporation) ~16 h before imaging. Cells were maintained at 37 °C in 5% CO<sub>2</sub> during live-cell imaging using a Zeiss XLmulti S1stage-top incubator. Images were collected on a Carl Zeiss Axio Observer Z1 motorized inverted microscope (Carl Zeiss MicroImaging) equipped with a Yokogawa CSU-X1 spinning-disk confocal head (Yokogawa Electric), a plan-apochromat ×63/1.4 numerical aperture objective, 4 laser lines for excitation (405, 488, 561 and 639 nm), a DirectFRAP laser manipulation module to drive optogenetic activation and an Evolve EMCCD (Photometrics) driven by ZenBlue software. Time-lapse sequences of TagRFP or TagRFP-GARRE were acquired at 10-s intervals for 10 min using the 561 nm laser. The first ten frames were taken without PA-RAC1 activation. Then, local optogenetic activation of PA-RAC1 was achieved via pulses of 100 ms of illumination using the 488-nm laser (1% power) restricted to a 10-μm diameter ROI by the DirectFRAP module repeated before each remaining frame. At least ten cells were photoactivated, and each condition was repeated in at least two independent experiments. For quantitative analyses, original stacks were subjected to bleach correction using histogram matching and background subtraction using Fiji. The MFI ratio at the activated area was obtained by dividing the MFI inside the ROI by the MFI of the entire cell. A value close to 1 means that the TagRFP probe is evenly distributed in the cell while a value >1 means that the TagRFP probe is enriched at the activated site. This value was plotted as a function of time, with optogenetic activation starting at 100 s.

#### *Drosophila* cell culture, transfection and biochemical analyses

S2R+ cells were grown at 25 °C in M3 medium supplemented with 10% HI-FBS (Gibco) and 50 units ml<sup>-1</sup> of penicillin–streptomycin (Gibco) and transfected as previously described<sup>70</sup>. For some experiments, cells were pretreated 48 h before transfection with 6 μg per 24-well of double-stranded RNA (dsRNA) targeting either β-

galactosidase or *slik* 5' untranslated region (UTR) as previously described<sup>70</sup> to deplete Slik. For immunoprecipitations/pull-downs, cells were lysed 72 h later in NP-40 lysis buffer and processed as previously described<sup>70</sup>. GST pulldowns were carried out for 2 h on ice using glutathione agarose (Pierce). For analysis of Moe phosphorylation, cells were lysed in TLB buffer (40 mM HEPES, 1 mM EDTA, 120 mM NaCl, 10 mM NaPPi, 1% Triton-X-100, 0.10% SDS, 10% glycerol, 1× protease inhibitor cocktail (Roche Applied Science), 50 µM β-glycerophosphate, 1 mM NaVO<sub>4</sub>, 5 mM NaF, 120 µg ml<sup>-1</sup> AEBSF (Sigma) and 1×PhosSTOP.

#### NanoBiT complementation assays

To measure protein interactions in live cells, we used the NanoBiT System (Promega). S2R+ cells were plated in 24-well plates and transfected as described above. To activate Rho1, cells were transfected with 300 ng of *pMT.puro/RhoGEF64C* or empty *pMT.puro* plasmid. To measure Rho1 activity, cells were co-transfected with 120 ng of *pMT.puro/LgBiT-Rho1* and 300 ng of *pMT.puro/SmBiT-PKN<sup>G58A</sup>RBD*. To measure Rho1 interactions with Slik, cells were co-transfected with 120 ng of *pMT.puro/LgBiT-Rho1* and 300 ng of *pMT.puro/SmBiT-Slik*. To measure Slik interactions with cell membranes, cells were co-transfected with 300 ng each of *pMT.puro/LgBiT-Slik* and *pMT.puro/myr89-SmBiT*. To measure Slik dimerization, cells were co-transfected with 300 ng each of *pMT.puro/Slik-LgBiT* and *pMT.puro/Slik-SmBiT*. After 16–24 h, cells were induced<sup>70</sup> and split in quadruplicate into Cellstar 96-well microplates (white polystyrene, flat bottom; Greiner Bio-One International) and covered with adhesive plate seals. After 72 h, luciferase activity was assessed using a Nano-Glo Luciferase assay (Promega).

#### *Drosophila* experiments

The *Drosophila* strains used are described in Supplementary Table 6. For overexpression for Rho1, *ptc-Gal4,UAS-GFP<sup>S65T</sup>;tub-gal80<sup>ts</sup>/TM6* virgin females were crossed to *w<sup>1118</sup>* or *UAS-Rho1* males at 25 °C. Vials with 0–2-day-old offspring were transferred to 18 °C for 5 days. Rho1 expression was initiated by transferring the vials to 27 °C to inactivate the temperature-sensitive Gal80<sup>ts</sup>. Larvae were collected 18–24 h later and anterior halves dissected and then processed for staining as previously

described<sup>70</sup>. Mounted coverslips were imaged using a Zeiss LSM700 confocal microscope. Fluorescence signals were quantified using Image J.

### Statistics and reproducibility

All mean  $\pm$  s.d. values were derived using Prism (GraphPad Software) or Microsoft Excel. The reproducibility of the results and sample sizes are mentioned in each corresponding figure legends. For high-content imaging for siRNA screening of RHOG<sup>G12V</sup>, statistical significance was determined using Student *t*-tests or one-way analysis of variance (ANOVA), followed by Bonferroni's multiple comparison test performed using Prism Software. *P* values  $<0.05$  were considered significant for all analyses (\**P*  $< 0.05$ , \*\**P*  $< 0.001$ , \*\*\**P*  $< 0.0001$ ). For p-ERM quantification, statistical significance was determined using nonparametric Mann–Whitney tests with a confidence interval of 95% performed using Prism Software. For NanoBiT complementation assays, statistical significance was determined using two-sided Student *t*-tests using Microsoft Excel Software.

### Reporting Summary

Further information on research design is available in the [Nature Research Reporting Summary](#) linked to this article.

### Data availability

---

The raw proteomics data have been deposited into ProteomeXchange (<http://www.proteomexchange.org>) with accession number [PXD015918](#). The BiOID data in this manuscript can also be explored in the supplementary tables and on a dedicated website ([http://prohits-web.lunenfeld.ca/GIPR/Datasets.php?projectID=25&m\\_num=m3](http://prohits-web.lunenfeld.ca/GIPR/Datasets.php?projectID=25&m_num=m3)). Source data for Figs. 2–8 and Extended Data Figs. 1 and 4–6 are available online. All data that support the findings of this study are available from the corresponding author upon reasonable request.

### Change history

---

**10 February 2020** A Correction to this paper has been published:

<https://doi.org/10.1038/s41556-020-0479-y>

## References

---

1. Rojas, A. M., Fuentes, G., Rausell, A. & Valencia, A. The Ras protein superfamily: evolutionary tree and role of conserved amino acids. *J. Cell Biol.* **196**, 189–201 (2012).
  2. Hodge, R. G. & Ridley, A. J. Regulating Rho GTPases and their regulators. *Nat. Rev. Mol. Cell Biol.* **17**, 496–510 (2016).
  3. Cherfils, J. & Zeghouf, M. Regulation of small GTPases by GEFs, GAPs, and GDIs. *Physiol. Rev.* **93**, 269–309 (2013).
  4. Laurin, M. & Cote, J. F. Insights into the biological functions of Dock family guanine nucleotide exchange factors. *Genes Dev.* **28**, 533–547 (2014).
  5. Rossman, K. L., Der, C. J. & Sondek, J. GEF means go: turning on RHO GTPases with guanine nucleotide-exchange factors. *Nat. Rev. Mol. Cell Biol.* **6**, 167–180 (2005).
  6. Tcherkezian, J. & Lamarche-Vane, N. Current knowledge of the large RhoGAP family of proteins. *Biol. Cell* **99**, 67–86 (2007).
  7. Mott, H. R. & Owen, D. Structures of Ras superfamily effector complexes: what have we learnt in two decades? *Crit. Rev. Biochem. Mol. Biol.* **50**, 85–133 (2015).
-

8. Olson, M. F. Rho GTPases, their post-translational modifications, disease-associated mutations and pharmacological inhibitors. *Small GTPases* **9**, 203–215 (2018).

---

9. Krauthammer, M. et al. Exome sequencing identifies recurrent somatic *RAC1* mutations in melanoma. *Nat. Genet.* **44**, 1006–1014 (2012).

---

10. Yoo, H. Y. et al. A recurrent inactivating mutation in RHOA GTPase in angioimmunoblastic T cell lymphoma. *Nat. Genet.* **46**, 371–375 (2014).

---

11. Heasman, S. J. & Ridley, A. J. Mammalian Rho GTPases: new insights into their functions from in vivo studies. *Nat. Rev. Mol. Cell Biol.* **9**, 690–701 (2008).

---

12. Mueller, P. M. et al. Spatial Organization of Rho GTPase signaling by RhoGEF/RhoGAP proteins. Preprint at *bioRxiv* <https://www.biorxiv.org/content/10.1101/354316v3> (2018).

---

13. Gingras, A. C., Abe, K. T. & Raught, B. Getting to know the neighborhood: using proximity-dependent biotinylation to characterize protein complexes and map organelles. *Curr. Opin. Chem. Biol.* **48**, 44–54 (2019).

---

14. Roux, K. J., Kim, D. I., Raida, M. & Burke, B. A promiscuous biotin ligase fusion protein identifies proximal and interacting proteins in mammalian cells. *J. Cell Biol.* **196**, 801–810 (2012).

---

15. Lai, C. C., Boguski, M., Broek, D. & Powers, S. Influence of guanine nucleotides on complex formation between Ras and CDC25 proteins. *Mol. Cell. Biol.* **13**, 1345–1352 (1993).

---

16. Garrett, M. D., Self, A. J., van Oers, C. & Hall, A. Identification of distinct cytoplasmic targets for ras/R-ras and rho regulatory proteins. *J. Biol. Chem.* **264**, 10–13 (1989).
- 
17. Youn, J. Y. et al. High-density proximity mapping reveals the subcellular organization of mRNA-associated granules and bodies. *Mol. Cell* **69**, 517–532.e11 (2018).
- 
18. Gupta, G. D. et al. A dynamic protein interaction landscape of the human centrosome–cilium interface. *Cell* **163**, 1484–1499 (2015).
- 
19. Couzens, A. L. et al. Protein interaction network of the mammalian Hippo pathway reveals mechanisms of kinase-phosphatase interactions. *Sci. Signal.* **6**, rs15 (2013).
- 
20. St-Denis, N. et al. Phenotypic and interaction profiling of the human phosphatases identifies diverse mitotic regulators. *Cell Rep.* **17**, 2488–2501 (2016).
- 
21. Eden, S., Rohatgi, R., Podtelejnikov, A. V., Mann, M. & Kirschner, M. W. Mechanism of regulation of WAVE1-induced actin nucleation by Rac1 and Nck. *Nature* **418**, 790–793 (2002).
- 
22. Tyler, J. J., Allwood, E. G. & Ayscough, K. R. WASP family proteins, more than Arp2/3 activators. *Biochem. Soc. Trans.* **44**, 1339–1345 (2016).
-

23. Ishizaki, T. et al. The small GTP-binding protein Rho binds to and activates a 160 kDa Ser/Thr protein kinase homologous to myotonic dystrophy kinase. *EMBOJ.* **15**, 1885–1893 (1996).

---

24. Rose, R. et al. Structural and mechanistic insights into the interaction between Rho and mammalian Dia. *Nature* **435**, 513–518 (2005).

---

25. Glaven, J. A., Whitehead, I. P., Nomanbhoy, T., Kay, R. & Cerione, R. A. Lfc and Lsc oncoproteins represent two new guanine nucleotide exchange factors for the Rho GTP-binding protein. *J. Biol. Chem.* **271**, 27374–27381 (1996).

---

26. Ren, Y., Li, R., Zheng, Y. & Busch, H. Cloning and characterization of GEF-H1, a microtubule-associated guanine nucleotide exchange factor for Rac and Rho GTPases. *J. Biol. Chem.* **273**, 34954–34960 (1998).

---

27. Xie, X., Chang, S. W., Tatsumoto, T., Chan, A. M. & Miki, T. TIM, a Dbl-related protein, regulates cell shape and cytoskeletal organization in a Rho-dependent manner. *Cell Signal.* **17**, 461–471 (2005).

---

28. Mitin, N., Rossman, K. L. & Der, C. J. Identification of a novel actin-binding domain within the Rho guanine nucleotide exchange factor TEM4. *PLoS ONE* **7**, e41876 (2012).

---

29. Rodrigues, N. R. et al. Characterization of *Ngef*, a novel member of the Dbl family of genes expressed predominantly in the caudate nucleus. *Genomics* **65**, 53–61 (2000).

---

30. Miki, T., Smith, C. L., Long, J. E., Eva, A. & Fleming, T. P. Oncogene *ect2* is related to regulators of small GTP-binding proteins. *Nature* **362**, 462–465 (1993).
- 
31. Zheng, Y., Olson, M. F., Hall, A., Cerione, R. A. & Toksoz, D. Direct involvement of the small GTP-binding protein Rho in *lbc* oncogene function. *J. Biol. Chem.* **270**, 9031–9034 (1995).
- 
32. Shinohara, M. et al. SWAP-70 is a guanine-nucleotide-exchange factor that mediates signalling of membrane ruffling. *Nature* **416**, 759–763 (2002).
- 
33. Brugnera, E. et al. Unconventional Rac-GEF activity is mediated through the Dock180–ELMO complex. *Nat. Cell Biol.* **4**, 574–582 (2002).
- 
34. Cote, J. F. & Vuori, K. Identification of an evolutionarily conserved superfamily of DOCK180-related proteins with guanine nucleotide exchange activity. *J. Cell Sci.* **115**, 4901–4913 (2002).
- 
35. Yajnik, V. et al. DOCK4, a GTPase activator, is disrupted during tumorigenesis. *Cell* **112**, 673–684 (2003).
- 
36. Vives, V. et al. The Rac1 exchange factor Dock5 is essential for bone resorption by osteoclasts. *J. Bone Miner. Res.* **26**, 1099–1110 (2011).
- 
37. Miyamoto, Y., Yamauchi, J., Sanbe, A. & Tanoue, A. Dock6, a Dock-C subfamily guanine nucleotide exchanger, has the dual specificity for Rac1 and Cdc42 and regulates neurite outgrowth. *Exp. Cell Res.* **313**, 791–804 (2007).

- 38.** Salazar, M. A. et al. Tuba, a novel protein containing Bin/amphiphysin/Rvs and Dbl homology domains, links dynamin to regulation of the actin cytoskeleton. *J. Biol. Chem.* **278**, 49031–49043 (2003).
- 
- 39.** Abiko, H. et al. Rho guanine nucleotide exchange factors involved in cyclic-stretch-induced reorientation of vascular endothelial cells. *J. Cell Sci.* **128**, 1683–1695 (2015).
- 
- 40.** Harada, Y. et al. DOCK8 is a Cdc42 activator critical for interstitial dendritic cell migration during immune responses. *Blood* **119**, 4451–4461 (2012).
- 
- 41.** Gadea, G., Sanz-Moreno, V., Self, A., Godi, A. & Marshall, C. J. DOCK10-mediated Cdc42 activation is necessary for amoeboid invasion of melanoma cells. *Curr. Biol.* **18**, 1456–1465 (2008).
- 
- 42.** Abe, K. et al. Vav2 is an activator of Cdc42, Rac1, and RhoA. *J. Biol. Chem.* **275**, 10141–10149 (2000).
- 
- 43.** Bellanger, J. M. et al. The two guanine nucleotide exchange factor domains of Trio link the Rac1 and the RhoA pathways in vivo. *Oncogene* **16**, 147–152 (1998).
- 
- 44.** Fukuhara, S., Murga, C., Zohar, M., Igishi, T. & Gutkind, J. S. A novel PDZ domain containing guanine nucleotide exchange factor links heterotrimeric G proteins to Rho. *J. Biol. Chem.* **274**, 5868–5879 (1999).
- 
- 45.** Yamauchi, J., Miyamoto, Y., Chan, J. R. & Tanoue, A. ErbB2 directly activates the exchange factor Dock7 to promote Schwann cell migration. *J. Cell Biol.* **181**, 351–365 (2008).

46. Manser, E. et al. PAK kinases are directly coupled to the PIX family of nucleotide exchange factors. *Mol. Cell* **1**, 183–192 (1998).
- 
47. Zhuang, B., Su, Y. S. & Sockanathan, S. FARP1 promotes the dendritic growth of spinal motor neuron subtypes through transmembrane Semaphorin6A and PlexinA4 signaling. *Neuron* **61**, 359–372 (2009).
- 
48. Chuang, T. H. et al. Abr and Bcr are multifunctional regulators of the Rho GTP-binding protein family. *Proc. Natl Acad. Sci. USA* **92**, 10282–10286 (1995).
- 
49. Ellerbroek, S. M. et al. SGEF, a RhoG guanine nucleotide exchange factor that stimulates macropinocytosis. *Mol. Biol. Cell* **15**, 3309–3319 (2004).
- 
50. Reuther, G. W. et al. Leukemia-associated Rho guanine nucleotide exchange factor, a Dbl family protein found mutated in leukemia, causes transformation by activation of RhoA. *J. Biol. Chem.* **276**, 27145–27151 (2001).
- 
51. Nguyen, T. T. et al. PLEKHG3 enhances polarized cell migration by activating actin filaments at the cell front. *Proc. Natl Acad. Sci. USA* **113**, 10091–10096 (2016).
- 
52. Amin, E. et al. Deciphering the molecular and functional basis of RHOGAP family proteins: a systematic approach toward selective inactivation of Rho family proteins. *J. Biol. Chem.* **291**, 20353–20371 (2016).
- 
53. Lamarche-Vane, N. & Hall, A. CdGAP, a novel proline-rich GTPase-activating protein for Cdc42 and Rac. *J. Biol. Chem.* **273**, 29172–29177 (1998).

54. Chen, P. W., Jian, X., Yoon, H. Y. & Randazzo, P. A. ARAP2 signals through Arf6 and Rac1 to control focal adhesion morphology. *J. Biol. Chem.* **288**, 5849–5860 (2013).
- 
55. Toure, A. et al. MgcRacGAP, a new human GTPase-activating protein for Rac and Cdc42 similar to *Drosophila rotundRacGAP* gene product, is expressed in male germ cells. *J. Biol. Chem.* **273**, 6019–6023 (1998).
- 
56. Wells, C. D. et al. A Rich1/Amot complex regulates the Cdc42 GTPase and apical-polarity proteins in epithelial cells. *Cell* **125**, 535–548 (2006).
- 
57. Omelchenko, T. & Hall, A. Myosin-IXA regulates collective epithelial cell migration by targeting RhoGAP activity to cell–cell junctions. *Curr. Biol.* **22**, 278–288 (2012).
- 
58. Myagmar, B. E. et al. PARG1, a protein-tyrosine phosphatase-associated RhoGAP, as a putative Rap2 effector. *Biochem. Biophys. Res. Commun.* **329**, 1046–1052 (2005).
- 
59. Wennerberg, K. et al. Rnd proteins function as RhoA antagonists by activating p190 RhoGAP. *Curr. Biol.* **13**, 1106–1115 (2003).
- 
60. Lo, H. F. et al. Association of dysfunctional synapse defective 1 (SYDE1) with restricted fetal growth–SYDE1 regulates placental cell migration and invasion. *J. Pathol.* **241**, 324–336 (2017).
- 
61. Katoh, H. & Negishi, M. RhoG activates Rac1 by direct interaction with the Dock180-binding protein Elmo. *Nature* **424**, 461–464 (2003).

62. Chenette, E. J., Abo, A. & Der, C. J. Critical and distinct roles of amino- and carboxyl-terminal sequences in regulation of the biological activity of the Chp atypical Rho GTPase. *J. Biol. Chem.* **280**, 13784–13792 (2005).
- 
63. Spektor, A., Tsang, W. Y., Khoo, D. & Dynlacht, B. D. Cep97 and CP110 suppress a cilia assembly program. *Cell* **130**, 678–690 (2007).
- 
64. Wu, Y. I. et al. A genetically encoded photoactivatable Rac controls the motility of living cells. *Nature* **461**, 104–108 (2009).
- 
65. Bashaw, G. J., Hu, H., Nobes, C. D. & Goodman, C. S. A novel Dbl family RhoGEF promotes Rho-dependent axon attraction to the central nervous system midline in Drosophila and overcomes Robo repulsion. *J. Cell Biol.* **155**, 1117–1122 (2001).
- 
66. Hipfner, D. R., Keller, N. & Cohen, S. M. Slik sterile-20 kinase regulates moesin activity to promote epithelial integrity during tissue growth. *Genes Dev.* **18**, 2243–2248 (2004).
- 
67. Viswanatha, R., Ohouo, P. Y., Smolka, M. B. & Bretscher, A. Local phosphocycling mediated by LOK/SLK restricts ezrin function to the apical aspect of epithelial cells. *J. Cell Biol.* **199**, 969–984 (2012).
- 
68. Matsui, T., Yonemura, S., Tsukita, S. & Tsukita, S. Activation of ERM proteins in vivo by Rho involves phosphatidyl-inositol 4-phosphate 5-kinase and not ROCK kinases. *Curr. Biol.* **9**, 1259–1262 (1999).

69. Hebert, M. et al. Rho-ROCK-dependent ezrin–radixin–moesin phosphorylation regulates Fas-mediated apoptosis in Jurkat cells. *J. Immunol.* **181**, 5963–5973 (2008).
- 
70. Panneton, V. et al. Regulation of catalytic and non-catalytic functions of the *Drosophila* Ste20 kinase Slik by activation segment phosphorylation. *J. Biol. Chem.* **290**, 20960–20971 (2015).
- 
71. Kovalski, J. R. et al. The functional proximal proteome of oncogenic *Ras* includes mTORC2. *Mol. Cell* **73**, 830–844.e12 (2019).
- 
72. Paul, F. et al. Quantitative GTPase affinity purification identifies Rho family protein interaction partners. *Mol. Cell. Proteomics* **16**, 73–85 (2017).
- 
73. Patel, M., Chiang, T. C., Tran, V., Lee, F. J. & Cote, J. F. The Arf family GTPase Arl4A complexes with ELMO proteins to promote actin cytoskeleton remodeling and reveals a versatile Ras-binding domain in the ELMO proteins family. *J. Biol. Chem.* **286**, 38969–38979 (2011).
- 
74. Methot, S. P. et al. A licensing step links AID to transcription elongation for mutagenesis in B cells. *Nat. Commun.* **9**, 1248 (2018).
- 
75. Liu, G. et al. Using ProHits to store, annotate, and analyze affinity purification-mass spectrometry (AP-MS) data. *Curr. Protoc. Bioinformatics* **39**, 8.16.1–8.16.32 (2012).
- 
76. Tyanova, S. et al. The Perseus computational platform for comprehensive analysis of (prote)omics data. *Nat. Methods* **13**, 731–740 (2016).

77. Knight, J. D. R. et al. ProHits-viz: a suite of web tools for visualizing interaction proteomics data. *Nat. Methods* **14**, 645–646 (2017).
- 
78. Findlay, S. et al. SHLD2/FAM35A co-operates with REV7 to coordinate DNA double-strand break repair pathway choice. *EMBOJ.* **37**, e100158 (2018).
- 
79. Meller, J., Vidali, L. & Schwartz, M. A. Endogenous RhoG is dispensable for integrin-mediated cell spreading but contributes to Rac-independent migration. *J. Cell Sci.* **121**, 1981–1989 (2008).

## Acknowledgements

---

The authors thank A. Echard (Institut Pasteur, France), O. Rocks (Max-Delbrueck-Center for Molecular Medicine, Germany), L. Sabourin (OHRI, Canada) for providing plasmids and antibodies. They also acknowledge the gift of Flp-In T-REx HeLa cells from S. Taylor (University of Manchester, UK). They also thank A. Pelletier, M. Tucholska and K. Oh for excellent technical assistance and J.-P. Lambert for helpful suggestions on data analyses. They thank the IRCM Proteomics facility for the processing of MS samples, C. Poitras for installing ProHits, and D. Filion, É. Lécuyer and X. Wang for microscopy assistance. This work was supported by operating grants from the National Science and Engineering Research Council of Canada (RGPIN-2017-05819 to D.R.H.; RGPIN-2016-04808 to J.-F.C) and the Canadian Institutes of Health Research (FDN144301 to A.-C.G.; H.B., N.S., I.E.E. and V.T. were recipients of FRQS Doctoral studentships). I.E.E. was also supported by an IRCM Foundation-TD scholarship. J.-F.C. holds the Transat Chair in Breast Cancer Research.

## Author information

---

These authors contributed equally: David R. Hipfner, Anne-Claude Gingras.

## Authors and Affiliations

**Montreal Clinical Research Institute (IRCM), Montréal, Québec, Canada**

Halil Bagci, Neera Sriskandarajah, Amélie Robert, Jonathan Boulais, Islam E. Elkholi, Viviane Tran, Marie-Pier Thibault, Nadia Dubé, Denis Faubert, David R. Hipfner & Jean-François Côté

#### **Department of Anatomy and Cell Biology, McGill University, Montréal, Québec, Canada**

Halil Bagci & Jean-François Côté

#### **Division of Experimental Medicine, Department of Medicine, McGill University, Montréal, Québec, Canada**

Neera Sriskandarajah & David R. Hipfner

#### **Molecular Biology Programs, Université de Montréal, Montréal, Québec, Canada**

Islam E. Elkholi, David R. Hipfner & Jean-François Côté

#### **Department of Biochemistry and Molecular Medicine, Université de Montréal, Montréal, Québec, Canada**

Viviane Tran

#### **Lunenfeld-Tanenbaum Research Institute, Sinai Health System, Toronto, Ontario, Canada**

Zhen-Yuan Lin & Anne-Claude Gingras

#### **Department of Medicine, Université de Montréal, Montréal, Québec, Canada**

David R. Hipfner & Jean-François Côté

#### **Department of Molecular Genetics, University of Toronto, Toronto, Ontario, Canada**

Anne-Claude Gingras

### Contributions

J.-F.C., A.-C.G., D.R.H., N.D., H.B., A.R, J.B. and I.E.E. designed the research. H.B., N.S., A.R., J.B., I.E.E., V.T., Z.-Y.L., M.-P.T., N.D. and D.R.H. performed the research. H.B., N.S., A.R., J.B., I.E.E., N.D., D.F., D.R.H., A.-C.G. and J.-F.C. analysed the data. J.-F.C., A.R., J.B., H.B., D.R.H. and A.-C.G. wrote the paper with input from all other authors.

### Corresponding author

Correspondence to [Jean-François Côté](#).

### Ethics declarations

### Competing interests

The authors declare no competing interests.

### Additional information

**Publisher's note** Springer Nature remains neutral with regard to jurisdictional claims in published maps and institutional affiliations.

## Extended data

### Extended Data Fig. 1 Validation of BirA\*-Flag-RHO GTPases expression constructs.

(a) Immunoblots of lysates from Flp-In T-REx HEK293 cells expressing the indicated constructs after induction with tetracycline (Tet). (b) Immunoblots of lysates from Flp-In T-REx HeLa cells expressing the indicated constructs before (-) and after (+) induction with tetracycline. (c) Western blots show the expression of the indicated BirA\*-Flag-RHO GTPases as compared to their endogenous counterpart in Flp-In T-REx HeLa cells treated with tetracycline. GADPH was used as loading control. All the data presented in Extended Data Fig 1 are representative of three independent experiments. See unmodified scans in Unprocessed Blots Extended Data Fig. 1.

### Source data

### Extended Data Fig. 2 Functionality of the BirA\*-Flag-RHO GTPases constructs.

BirA\*-Flag-RHO GTPases induce cytoskeletal changes. Flp-In T-REx HeLa cell lines were treated with tetracycline together with biotin to induce the expression of the indicated BirA\*-Flag-RHO GTPases and the biotinylation of their proximal interactors. Confocal microscopy images of F-actin (Alexa Fluor 488-phalloidin) and biotin (Alexa Fluor 647-streptavidin) are shown. In comparison to control cells, expression of constitutively active RHO-subfamily led to the formation of thick stress fibres while expression of RAC-subfamily proteins promoted the development of large lamellipodia. Expression of the CDC42-subfamily proteins revealed different phenotypes with  $\text{CDC42}^{\text{G12V}}$  enhancing growth of filopodia while  $\text{RHOJ}^{\text{G40V}}$  and  $\text{RHOQ}^{\text{G18V}}$  promoting both membrane ruffles and filopodia formation. Expression of constitutively active versions of RHOD/F-subfamily proteins led to the formation of long filopodia. The constitutively active versions of the fast cycling atypical RHOU/V-subfamily, as well as  $\text{RHOH}^{\text{WT}}$ , induced the formation of both membrane ruffles and filopodia. The RND proteins did not mediate strong phenotypes with the exception that RND3 expressing cells showed less actin fibres. Finally, members from the RHOBTB-subfamily did not alter the cytoskeleton. Data are representative of two independent experiments. Bars, 10  $\mu\text{m}$ .

## Extended Data Fig. 3 The constitutively active forms of the RHO GTPases baits are more efficient than the corresponding wild type forms to identify GAPs and effectors.

The constitutively active forms of the RHO GTPases enrich more interactions than the corresponding WT forms to identify GAPs and effectors. SAINT express analyses were performed on the following sample sizes (number of interactions): n = 5381 for NF in HEK, n = 7462 for NF in HeLa, n = 17548 for Active in HEK and n = 22042 for Active in HeLa. Only proximity interactions displaying an AvgP  $\geq$  0.95 (below the Bayesian 1% FDR estimate) were kept and deemed of high confidence. (a) Enrichment of BioID interactions of well-known downstream effectors and complexes with the indicated RHO GTPases. (b) Enrichment of BioID interactions of RHOGAPs with the indicated RHO GTPases.

## Extended Data Fig. 4 Basic characterization of GARRE (KIAA0355).

(a) The Phylogenetic tree of GARRE orthologues shows its recent evolutionary origin. (b) PHYRE2 threading software identifies a BAR domain in GARRE similar to the BAR domain of Amphiphysin. Conserved amino acids are in red. (c) Schematic of GARRE displaying the location of the DUF4745 superfamily domain as revealed by amino acid Blast alignment of the GARRE sequence. Note that the DUF domain overlaps with the position of the BAR domain (in yellow). (d) GARRE has no GAP activity on RAC1. Active RAC1 was pulled-down using purified GST-PAK-PDB in cell lysates from HeLa cells expressing Flag-DOCK180 and/or Flag-GARRE. Data are representative of four independent experiments. See unmodified scans in Unprocessed Blots Extended Data Fig. 4.

### Source data

## Extended Data Fig. 5 A functional siRNA screen for the top RHO<sup>G12V</sup> BioID interactors.

A functional siRNA screen for the top RHO<sup>G12V</sup> BioID interactors reveals PLEKHG3 as an effector (a) Schematic illustration of the functional siRNA screening approach for RHOG. Flp-In T-REx HeLa cells expressing Flag-RHOG<sup>G12V</sup> in a tetracycline-inducible manner were transfected with a set of ON-target SmartPool siRNAs targeting the top 22 RHOG<sup>G12V</sup> BioID effectors prior to tetracycline induction of RHOG<sup>G12V</sup> and were

next subjected to anti-Flag and F-actin staining. Samples were analyzed using low-resolution high throughput microscopy and percentage of cells presenting RHOG<sup>G12V</sup> and F-actin-enriched membrane ruffles was quantified. (b) High-resolution confocal microscopy images show that RHOG<sup>WT</sup> induces multiple discrete ruffles while RHOG<sup>G12V</sup> causes the formation of a uniform membrane ruffle, which is inhibited by RAC1 siRNA. Data are representative of three independent experiments. Bar, 10  $\mu\text{m}$ . (c, d) Computational analyses of the cell shape reveal that the increase in circularity induced by RHOG<sup>G12V</sup> expression is inhibited by *RAC1*, *ELMO2* or *PLEKHG3* siRNA. A circularity value of 1.0 indicates a perfect circle. As the value approaches 0.0, it indicates an increasingly elongated polygon. (c) The graph shows the frequency distribution of circularity for control cells (expressing GFP or GFP<sup>-</sup>RHOG<sup>WT</sup>) in grey versus GFP-RHOG<sup>G12V</sup> expressing cells in black. ( $n = 377$  control cells or 220 RHOG<sup>G12V</sup>-expressing cells from 3 independent experiments). (d) The graph compares the frequency distribution of circularity of GFP-RHOG<sup>G12V</sup>-expressing cells 72 h after treatment with the indicated siRNAs. ( $n = 287$  cells for siControl, 363 cells for siRAC1, 382 for siELMO2 and 325 for siPLEHG3 from 3 independent experiments). See Statistical Source Data\_Extended Data Fig. 5.

## Source data

### Extended Data Fig. 6 Activation of ROCK1/2 downstream of RHOA contributes to ERM proteins phosphorylation.

(a) Western blot showing SLK, LOK and ROCK1 depletion after 72 h treatment with indicated siRNAs. Tubulin was used as a loading control. Data are representative of 2 independent experiments. (b) Confocal images of p-ERM staining in Flag-RHOA Flp-In T-REx HeLa cells before (control) or after induction with tetracycline for 16 h. Note that the treatment of RHOA<sup>G14V</sup>-expressing cells with the ROCK inhibitor Y-27632 (10  $\mu\text{M}$  for 30 min) was sufficient to reduce p-ERM. Data are representative of three independent experiments. Bar = 10  $\mu\text{m}$ . (c) Cells were treated as in b and p-ERM mean fluorescence intensity (MFI) was measured. The graph shows the mean + / - SD of the relative p-ERM MFI as compared to the control (Flag-RHOA Flp-In T-REx HeLa cells without tetracycline induction).  $n = 22$  images of control,  $n = 19$  images of RHOA<sup>WT</sup>,  $n = 22$  images of RHOA<sup>G14V</sup> and  $n = 25$  images of RHOA<sup>G14V</sup> + Y27632 from two

independent experiments (See Statistical Source Data Extended Data Fig. 5). P-value was calculated using the Mann-Whitney non-parametric two-tailed test \*\*\*\*, p < 0.0001.

## [Source data](#)

## **Supplementary information**

---

### [Reporting Summary](#)

### [Supplementary Video 1](#)

Lamellipodia formation following local PA-RAC1 photoactivation in TagRFP-expressing cells. Hela cells were transfected with PA-RAC1 together with TagRFP. The red arrow points to the membrane protrusion induced by PA-RAC1 activation by repeated local illumination with blue light (cyan circle). This video is associated with Fig. 4i (upper panel). Data are representative of two independent experiments.

### [Supplementary Video 2](#)

Recruitment of GARRE-TagRFP following the local photoactivation of PA-RAC1. Hela cells were transfected with PA-RAC1 together with GARRE-TagRFP. The yellow arrow points to the recruitment of GARRE-TagRFP into structures reminiscent of tubular membranes after PA-RAC1 activation by repeated local illumination with blue light (cyan circle). This video is associated with Fig. 4i (lower panel). Data are representative of two independent experiments.

### [Supplementary Tables](#)

Supplementary Tables 1–16.

### [Supplementary Data 1](#)

Cytoscape file (Cytoscape.org) containing the networks of every RHO GTPases in active or nucleotide free (NF) forms.

## **Source data**

---

### [Source Data Fig. 2](#)

Unprocessed Western Blots and/or gels

### **Source Data Fig. 3**

Unprocessed Western Blots and/or gels

### **Source Data Fig. 4**

Statistical Source Data

### **Source Data Fig. 4**

Unprocessed Western Blots and/or gels

### **Source Data Fig. 5**

Statistical Source Data

### **Source Data Fig. 5**

Unprocessed Western Blots and/or gels

### **Source Data Fig. 6**

Statistical Source Data

### **Source Data Fig. 6**

Unprocessed Western Blots and/or gels

### **Source Data Fig. 7**

Statistical Source Data

### **Source Data Fig. 7**

Unprocessed Western Blots and/or gels

### **Source Data Fig. 8**

Statistical Source Data

### **Source Data Fig. 8**

Unprocessed Western Blots and/or gels

### **Source Data Extended Data Fig. 1**

## Unprocessed Western Blots and/or gels

### Source Data Extended Data Fig.4

Unprocessed Western Blots and/or gels

### Source Data Extended Data Fig.5

Statistical Source Data

### Source Data Extended Data Fig.6

Statistical Source Data

### Source Data Extended Data Fig.6

Unprocessed Western Blots and/or gels

## Rights and permissions

---

### Reprints and Permissions

## About this article

---

### Cite this article

Bagci, H., Sriskandarajah, N., Robert, A. *et al.* Mapping the proximity interaction network of the Rho-family GTPases reveals signalling pathways and regulatory mechanisms. *Nat Cell Biol* **22**, 120–134 (2020). <https://doi.org/10.1038/s41556-019-0438-7>

#### Received

08 April 2019

#### Accepted

19 November 2019

#### Published

23 December 2019

#### Issue Date

01 January 2020

#### DOI

<https://doi.org/10.1038/s41556-019-0438-7>

### Share this article

Anyone you share the following link with will be able to read this content:

[Get shareable link](#)

Provided by the Springer Nature SharedIt content-sharing initiative

## Subjects

[Biochemistry](#) • [Biological techniques](#) • [Cell biology](#) • [Computational biology and bioinformatics](#) • [Molecular biology](#)

## This article is cited by

### [\*\*RHOJ controls EMT-associated resistance to chemotherapy.\*\*](#)

Maud Debaugnies, Sara Rodríguez-Acebes ... Cédric Blanpain

*Nature* (2023)

### [\*\*RhoGDI \$\alpha\$ regulates spermatogenesis through Rac1/cofilin/F-actin signaling\*\*](#)

Haixia Zhu, Zongzhuang Wen ... Jiangang Gao

*Communications Biology* (2023)

### [\*\*Role of RhoG as a regulator of cellular functions: integrating insights on immune cell activation, migration, and functions\*\*](#)

Shubham Kumar Rai, Divya Singh & Pranita P. Sarangi

*Inflammation Research* (2023)

### [\*\*MicroRNAs in atrial fibrillation target genes in structural remodelling\*\*](#)

Nicoline W. E. van den Berg, Makiri Kawasaki ... Joris R. de Groot

*Cell and Tissue Research* (2023)

### [\*\*Functional and molecular dissection of HCMV long non-coding RNAs\*\*](#)

Sungwon Lee, Hyewon Kim ... Kwangseog Ahn

*Scientific Reports* (2022)